nature communications

Article

https://doi.org/10.1038/s41467-025-64530-8

Experimental realization of temporal refraction and reflection in elastic beams

Received: 8 January 2025

Accepted: 17 September 2025

Shaoyun Wang[1,6], Nan Shao[1,6], Hui Chen[2], Jiaji Chen[1], Honghua Qian[1], Qian Wu[1], Huiling Duan[3], Andrea Alú[4,5] & Guoliang Huang[3]

Wave reflection and refraction at a time interface follow different conservation laws compared to conventional scattering at a spatial interface. This study presents the experimental demonstration of refraction and reflection of flexural waves across a temporal boundary in a continuum-based mechanical metabeam, and unveils opportunities that emerge by tailoring temporal scattering phenomena for phononic applications. We observe these phenomena in an elastic beam attached to an array of piezoelectric patches that can vary in time the effective elastic properties of the beam. Frequency conversion and phase conjugation are observed upon a single temporal interface. These results are consistent with the temporal Snell's law and Fresnel equations for temporal interfaces. Further, we illustrate the manipulation of amplitude and frequency spectra of flexural wave temporal refraction and reflection through multi-stepped temporal interfaces. Finally, by implementing a smooth time variation of wave impedance, we numerically and experimentally demonstrate the capabilities of the temporal metabeam to realize waveform morphing and information coding. Our findings enable precise control over wave amplitude and frequency through temporally modulated mechanical systems, providing a concrete framework for designing time-mechanical metamaterials and time-phononic crystals.

Wave propagation in time-varying media exhibits dynamics that are strikingly different from those in space-varying media[1–3]. The breaking of time translation symmetry allows energy exchange between the wave and the time-varying medium due to Noether's theorem[4,5], leading to phenomena such as frequency manipulation[6], wave amplification[7], and self-emission[8–10]. Additionally, the Kramers-Kronig relations, grounded in the principle of causality in time-varying systems, enable these systems to surpass well-established fundamental performance limits, including the Bode-Fano limit, Rozanov bound, and Chu limit[11–14].

Despite these differences, wave propagation in time-varying media and space-varying media shares notable analogies. Space-time duality suggests that phenomena observed in spatially varying systems generally have analogous temporal versions, and vice versa[15–17]. In suddenly varying systems, phenomena analogous to wave scattering at spatial interfaces—such as reflection and refraction[18–23], anti-reflection coatings[24], total internal reflection[25], Goos-Hänchen effect[26,27], wave holography[28], double slit diffraction[29], and photon collisions[30], can occur at temporal interfaces. Moreover, in periodic and disordered systems, temporal analogs such as time crystals[31–33], disordered time-varying media[34–36], *k*-bandgaps[37], the topology of *k*-bands and corresponding temporal interface modes[38], and *k*-gap solitons and breathers[39,40], are developed. In slowly (adiabatically) varying systems,

---

[1]Department of Mechanical and Aerospace Engineering, University of Missouri, Columbia, MO, USA. [2]Center for Mechanics Plus under Extreme Environments, School of Mechanical Engineering and Mechanics, Ningbo University, Ningbo, China. [3]Department of Mechanics and Engineering Science, College of Engineering, Peking University, Beijing, P R China. [4]Photonics Initiative, Advanced Science Research Center, City University of New York, New York, NY, USA. [5]Physics Program, Graduate Center, City University of New York, New York, NY, USA. [6]These authors contributed equally: Shaoyun Wang, Nan Shao.
✉e-mail: aalu@gc.cuny.edu; guohuang@pku.edu.cn

perfect state transitions such as controllable frequency shifts[41–43], topological state pumping[44,45], and non-Abelian braiding[46,47] are achieved in both space-varying and time-varying systems.

Among these phenomena, wave refraction and reflection at temporal interfaces are considered one of the most fundamental phenomena at the foundations of time crystals, yet they are often challenging to achieve in practical wave systems. One of the key challenges is the creation of a temporal boundary, which typically requires a spatially uniform, ultrafast, and large change of wave impedance[19,48]. The associated experimental challenges keep the experimental study of wave scattering at temporal interfaces in its infancy, particularly in the context of elastic media. Recently, the observation of temporal refraction and reflection has been reported for electromagnetic waves leveraging transmission-line metamaterials[19,21]. Building on this, temporal interfaces are demonstrated in discrete elastic systems using repelling magnets and electromagnetic control[49], but such platforms cannot be extended to continuum systems due to the slow response of electromagnetic actuation. In contrast, prior studies in elastic continua demonstrate smooth temporal stiffness-damping modulation for inducing amplitude modulation and spectral shaping[50], and periodic modulation for *k*-space bandgaps[37] and dynamic phononic crystal[51]. Unlike previous works, which employed stiffness modulation that is continuous, periodic, or slow, realizing a sharp and spatially uniform temporal interface remains elusive in continuum elastic media, primarily due to the strict requirements of sub-microsecond synchronization and uniform stiffness modulation across the entire structure. Although temporal Snell's law and Fresnel equations are well-established in optics and discrete elastic systems, no field-based formulation exists for continuum beams. Likewise, momentum conservation and the breakdown of energy conservation—concepts rooted in Noether's theorem—are not formulated in time-varying beam theory. Furthermore, the use of sharp temporal interfaces for simultaneous and broadband manipulation of multiple wave attributes—frequency, amplitude, and phase—remains largely unexplored in elastic media.

Elastic beams, equipped with piezoelectric patches connected to digital and analog circuits, provide an excellent platform to achieve unconventional elastic wave phenomena, including the non-Hermitian skin effect[52], odd mass density[53], Willis responses[54], frequency conversion[55], and topological pumping[56]. In this study, we report the experimental realization of a sharp temporal interface in an elastic beam, enabled by real-time, circuit-driven stiffness modulation at the sub-microsecond scale using piezoelectric patches. Specifically, we implement sudden transitions between electrical boundary conditions by precisely controlling the switching of shunted circuits in sub-microsecond resolution (0.1 μs). This setup allows the direct observation of temporal refraction and reflection of flexural waves to address a long-standing experimental challenge in the field. We further derive temporal Snell's law and Fresnel equations for flexural waves directly from the governing equations of motion and formulate momentum conservation and the breakdown of energy conservation in time-varying elastic systems using Noether's theorem. These theoretical developments are further validated through numerical simulation and experimental observation, enabled by the ultrafast, broadband, and programmable stiffness modulation. By introducing multiple temporal interfaces, we demonstrate further control over the manipulation of flexural waves in both amplitude and frequency spectra, which have not been explored before. Finally, by programming a smooth time-varying transfer function to realize adiabatic stiffness modulations, we demonstrate additional capabilities in shaping the time-scattered waves in periodic and aperiodic fashion for smart waveform morphing and information coding. These results not only establish a programmable platform for manipulating elastic waves in practical engineering systems but also deepen the fundamental understanding of wave-matter interactions under temporal modulation.

Results

A time-varying metabeam supporting temporal interfaces

The time-varying metamaterial under analysis consists of a long, thin beam where bending is the primary mode of deformation. Each unit cell of this metabeam is equipped with a piezoelectric patch that senses bending deformation and provides a self-response. The patch acts as a sensor by generating a voltage proportional to the elongation or contraction of the beam's top surface (see Fig. 1a). The time-dependent transfer function, $H(t)$, comprises an analog switch, a microcontroller, and a time-varying digital potentiometer $R_1(t)$, defined as $H(t) = R_1(t)/$

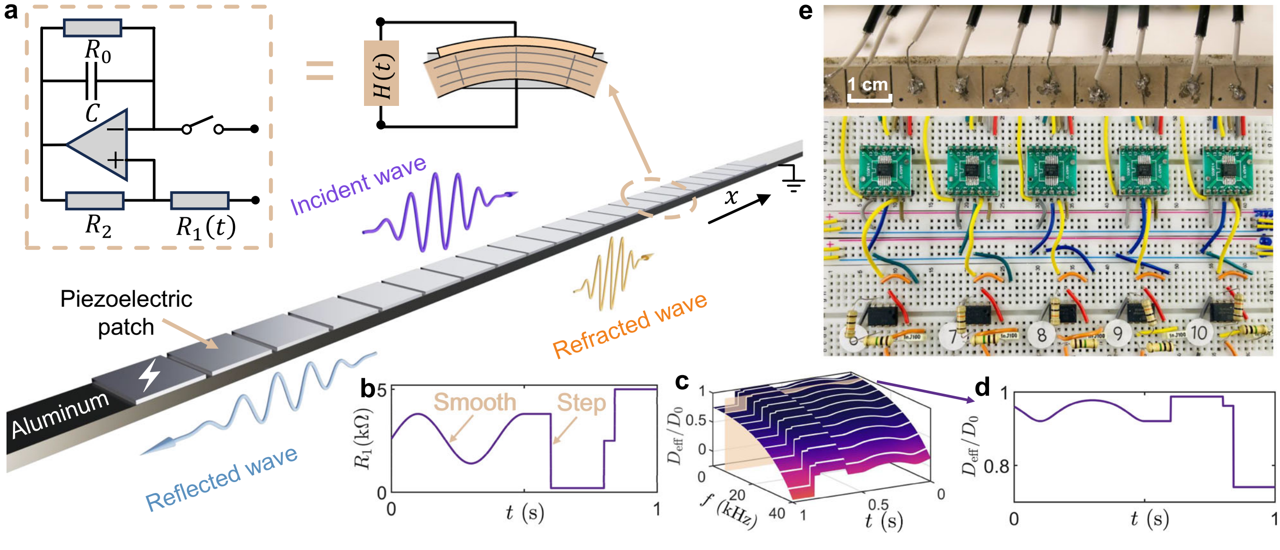

Fig. 1 | Design of a time-varying metabeam. a A segment of the time-varying metabeam designed to enable temporal scattering phenomena, such as temporal refraction and reflection, includes a unit cell equipped with a piezoelectric patch and voltage excitation (lighting sign), where the time-varying transfer function is implemented using an electric circuit network. **b** A plot illustrating a time-varying transfer function $H(t)$, which includes both smooth and step changes over time. **c** A graph showing the variation in effective bending stiffness as a function of both frequency f and time t, based on the time-varying transfer function $H(t)$ from (**b**). Here, the bending stiffness D_0 in open circuit status is 0.88 Nm^{-2}. **d** The effective bending stiffness $D(t)$ plotted over time along the gray dashed line in (**c**), illustrating its time-dependent behavior. **e** Photo of the metabeam connected with time-varying electronic circuits labeled in each unit cell.

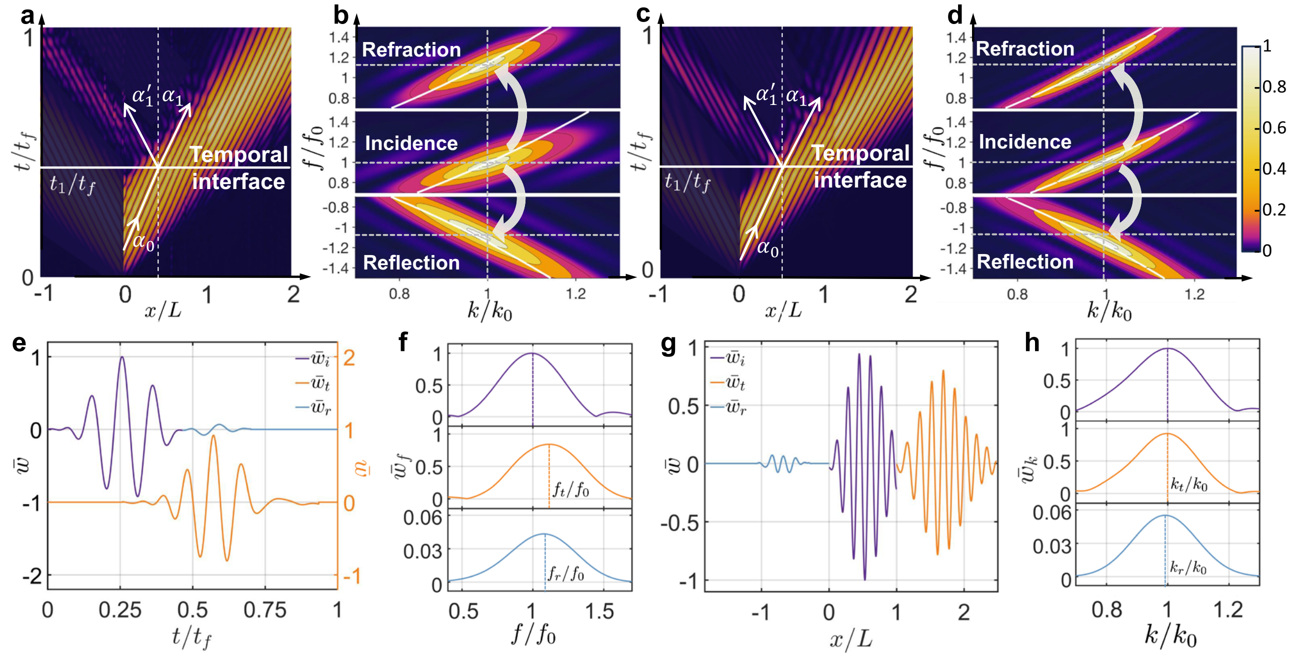

Fig. 2 | Refraction and reflection of flexural waves at a temporal interface. **a**, **c** The space-time diagram of experimental (**a**) and simulated (**c**) wave scattering at a temporal interface $t_1 = 0.44$ ms for an incident wave packet consisting of 3 cycles in the time domain with $t_f = 1.1$ ms. The metabeam is positioned within the interval (0, L), while the surrounding regions consist of an aluminum beam. The angles α_i, α_1, and α_1' represent the incident, refracted, and reflected angles, respectively. In **a**, these angles are 49°, 52°, and 52.5°, while in **c**, they are 47°, 50. 5°, and 51°. **b**, **d** The top, middle, and bottom panels display the experimental (**b**) and simulated (**d**) contour diagrams of the refracted, incident, and reflected waves, respectively. The data is obtained from a 2D Fourier transformation of the experimental and simulated data shown in (**a**) and (**c**). The incident frequency f_0 is 6.2 kHz and the incident wavenumber k_0 is 119 rad/m. The white lines indicate dispersion curves from unit cell analysis. **e** The normalized incident ($\bar{w}_i$) and reflected ($\bar{w}_r$) signals measured at $x/L = 0.05$, along with the refracted signal ($\bar{w}_t$) observed at $x/L = 1$. **f** Spectral analysis of the time-domain signals from (**e**). Here, f_0, f_t, and f_r are the spectral peak frequencies of incident, refracted, and reflected waves, respectively. **g** The incident spatial profile ($\bar{w}_i$) measured at $t/t_f = 1/3$, along with the refracted ($\bar{w}_t$) and reflected ($\bar{w}_r$) spatial profiles at $t/t_f = 2/3$. **h** Spectral analysis of the spatial-domain signals from (**g**). Here, k_0, k_t, and k_r are the spectral peak wavenumbers of incident, refracted, and reflected waves, respectively.

(R_2C)[57–59], as illustrated in Fig. 1b. As a result, the piezoelectric patch also serves as a mechanical actuator, elongating and contracting in response to the applied voltage, and thereby modifying the effective bending stiffness of the beam. To evaluate the performance of the metabeam, we numerically calculated the time-varying effective bending stiffness using COMSOL simulations (see Supplementary Section 1 for details). The resultant effective time-varying bending stiffness of the metabeam $D(t)$ across different frequencies and times can be found in Fig. 1c. Specifically, Fig. 1d illustrates the effective bending stiffness as a function of time for a particular frequency, intersected by the orange surface in Fig. 1c.

We conducted a thorough experimental investigation of the refraction and reflection of flexural waves at a temporal interface. We employ a one-dimensional metabeam controlled by a time-varying electric circuit network, as illustrated in Fig. 1e. The temporal interface is created by toggling the analog switch between ON and OFF states. When the switch is ON, R_1 is set to 5 kΩ, corresponding to a bending stiffness of 0.63 N m^{-2}. When the switch is OFF, R_1 becomes effectively infinite (∞), resulting in a bending stiffness of 0.88 N m^{-2}. In the experiment, a 3-cycle tone-burst signal with a central frequency of 6 kHz is applied at the left interface ($x/L = 0$) between the host beam and the modulated metabeam. The magnitude of the flexural wave field, $|w(x, t)|$, is measured throughout the system using a scanning laser Doppler vibrometer (Polytec PSV-400), as shown in Fig. 2a. At $t_1/t_f = 0.4$, the switch transitions from ON to OFF, creating a step-change boundary that causes a rapid shift in the bending stiffness of the modulated metabeam section. The switching time is 150 ns, ensuring an ideal temporal interface. Further details on the experimental setup can be found in the Methods and Supplementary Section 2. At the temporal interface, the incident wave splits into a temporally right-propagating refracted wave and a temporally left-propagating reflected wave. In this figure, only the temporal reflection is shown, with the left-propagating waves from incidence and spatial reflection at $x/L = 1$ removed (see details in Supplementary Section 3). We define the wavefront direction as the direction of wave propagation (see Fig. 2a, c). As such, the incident angle (49° in the experiment and 47° in the simulation) differs from both the refracted angle (52° in the experiment and 50. 5° in the simulation) and the reflected angle (52. 5° in the experiment and 51° in the simulation), indicating a change in wave direction. The Fourier transform in Fig. 2b illustrates the frequency bandwidth of the input and output waves resulting from temporal reflection and refraction. It shows that the normalized frequency of the incident wave shifts from 1 to 1.16 for refraction and to 1.13 for reflection, while the normalized wavenumbers remain constant. Numerical simulations are performed to validate our experimental observations, as shown in Fig. 2c, d. The results exhibit excellent agreement between the measured output frequencies after the temporal boundary and the numerical predictions, both in the time and frequency domains. To further verify the frequency conversion and wavenumber invariance, time-domain signals measured at $x/L = 0.05$ and $x/L = 1$ are shown in Fig. 2e, where three distinct wave packets corresponding to the incident, refracted, and reflected waves are clearly visible. The normalized frequency $f_t/f_0 = 1.15$ for the refracted wave and $f_r/f_0 = 1.11$ for the reflected wave quantitatively demonstrate the shift relative to the input frequency of the incident wave, as shown in Fig. 2f, indicating a breakdown of energy conservation. Additionally, the spatial-domain signals measured at $t/t_f = 1/3$ and $t/t_f = 2/3$ are shown in Fig. 2g. The wavenumbers k_t for the refracted wave and k_r for the reflected wave are consistent with the wavenumber k_0 of the incident wave, as depicted in Fig. 2h, demonstrating the conservation of momentum. The corresponding numerical results for

Fig. 2e–h are provided in Supplementary Section 4. Further results on wave refraction and reflection during the switch from OFF to ON at different frequencies are provided in Supplementary Sections 5 and 6. The effect of finite switching time on wave refraction and reflection is discussed in Supplementary Section 7. To rule out spatial reflection, we simulate an asymmetric pair of wave packets, resulting in a reversed order of the reflected waves (see Supplementary Section 8 for details).

Refraction and reflection of the flexural wave at a temporal interface

To understand frequency conversion through a temporal interface, we theoretically analyze flexural wave scattering at a temporal interface. In the absence of external forces, the behavior of flexural waves is governed by the Euler-Bernoulli beam equation with time-dependent bending stiffness, expressed as:

$$\frac{\partial}{\partial t}\left(\rho A \frac{\partial w(x,t)}{\partial t}\right) + \frac{\partial^2}{\partial x^2}\left(D(t)\frac{\partial^2 w(x,t)}{\partial x^2}\right) = 0, \tag{1}$$

where $D = EI$ represents the bending stiffness, E is Young's modulus, and I is the second moment of area. Additionally, ρ denotes the density, and A represents the beam's cross-sectional area. For temporal refraction and reflection, the bending stiffness is modulated as a step function over time: $D(t) = D_0 + (D_1 - D_0)\Theta(t - t_1)$, where $\Theta(t)$ is the Heaviside step function, D_0 represents the initial bending stiffness, and D_1 denotes the bending stiffness after an abrupt change at time $t = t_1$. The conditions for temporal continuity, outlined in Supplementary Section 9, guarantee the smooth transition of both momentum and displacement at the temporal interface without external forces. These conditions are formulated as follows:

$$\rho A \left.\frac{\partial w}{\partial t}\right|_{t=t_1^+} = \rho A \left.\frac{\partial w}{\partial t}\right|_{t=t_1^-}, \quad w|_{t=t_1^+} = w|_{t=t_1^-}. \tag{2}$$

Here, continuity conditions are applied to momentum and displacement fields, in analogy to the continuity of electric displacement **D** and magnetic flux density **B** in electrodynamics[2]. In our system, the absence of impulses ensures the continuity of momentum. Meanwhile, the invariance of density leads to the continuity of the velocity field, which, in turn, ensures the continuity of the displacement field.

The bending stiffness in Eq. (1) is constant in time at all instances, except at the time interface. Therefore, the wave obeys the conventional expressions stemming from the separation of variables both before and after the time interface. For medium 1 ($t < t_1$), the solution for the incident wave, based on Eq. (1), can be expressed as:

$$w = A_i e^{ik_0 x - i\omega_0 t}, \quad t < t_1, \tag{3}$$

where A_i is the incident wave coefficient, and the angular frequency Ω_0 and wavenumber k_0 before the switching event satisfy the dispersion relation $\omega_0 = \sqrt{D_0/(\rho A)}k_0^2$. For medium 2 ($t > t_1$), the displacement field, composed of the refracted and reflected waves after the switching event, can be expressed as:

$$w = \left[T e^{-i\omega_1(t-t_1)} + R e^{i\omega_1(t-t_1)}\right] A_i e^{i(k_1 x - \omega_0 t_1)}, \quad t > t_1, \tag{4}$$

where T is the refraction coefficient, and R is the reflection coefficient. The angular frequency Ω_1 and wavenumber k_1 after the switching event are related by the equation $\omega_1 = \sqrt{D_1/(\rho A)}k_1^2$. By inserting the wave solutions from Eqs. (3) and (4) into the temporal continuity conditions given by Eq. (2), we obtain

$$\begin{aligned} e^{ik_0 x} &= (T + R)e^{ik_1 x}, \\ -i\omega_0 e^{ik_0 x} &= (-i\omega_1 T + i\omega_1 R)e^{ik_1 x}. \end{aligned} \tag{5}$$

The temporal continuity conditions in Eq. (5) are satisfied at every point in space, which requires

$$k_1 = k_0, \tag{6}$$

or equivalently

$$\omega_1 n_1 = \omega_0 n_0, \tag{7}$$

where the elastic index of refraction is defined as $n_j = \sqrt{\rho A / D_j}$, with $j = 0, 1$ representing the different media before and after the switching event. Eq. (7) can be interpreted as the temporal Snell's law. Given the frequency of the incident wave and the refractive indices before and after the switching event, the frequency of the refracted wave can be predicted using Eq. (7). The more familiar form, which describes the geometric relationship between the angles of the incident and refracted waves in a space-time diagram, is given by

$$\frac{\tan\alpha_1}{\tan\alpha_0} = \frac{n_0}{n_1}, \tag{8}$$

where α_0 is the incident angle and α_1 is the refracted angle. See Supplementary Section 10 for the detailed derivation.

By substituting Eq. (6) and Eq. (7) into Eq. (5), we can obtain the temporal scattering coefficients as

$$R = \frac{1}{2}\left(1 - \frac{Z_0}{Z_1}\right), \quad T = \frac{1}{2}\left(1 + \frac{Z_0}{Z_1}\right), \tag{9}$$

where $Z_j = \sqrt{\rho A D_j}$ with $j = 0, 1$ represents the elastic impedance. Eq. (9) serves as the analog of Fresnel equations at the temporal interface, predicting the amplitudes of the refracted and reflected waves. The above derivation is based on the Euler–Bernoulli model, which considers only bending deformation. A detailed justification for neglecting shear deformation (via the Timoshenko beam model), as well as the negligible influence of higher-order flexural modes, longitudinal modes, damping, and nonlinear effects, is provided in Supplementary Section 11.

At a temporal interface, time-translation symmetry is broken, leading to the breakdown of energy conservation according to Noether's theorem. In Supplementary Section 12, the total energy of the elastic beam is given by

$$H = \int dx \left(\frac{1}{2}\rho A, \partial_t w^\dagger(x,t)\partial_t w(x,t) + \frac{1}{2}EI, \partial_{xx} w^\dagger(x,t)\partial_{xx} w(x,t)\right), \tag{10}$$

where † denotes the Hermitian conjugate. Before the temporal interface, the energy is

$$H_0 = \frac{1}{Z_0^2}\rho A A_i^2, \tag{11}$$

and after the interface it becomes

$$H_1 = \frac{Z_0^4 + Z_0^2 Z_1^2}{2Z_1^4} H_0, \tag{12}$$

which differs from H_0 when $Z_1 \neq Z_0$.

By contrast, the system preserves space-translation invariance, ensuring that momentum is conserved. This conserved momentum,

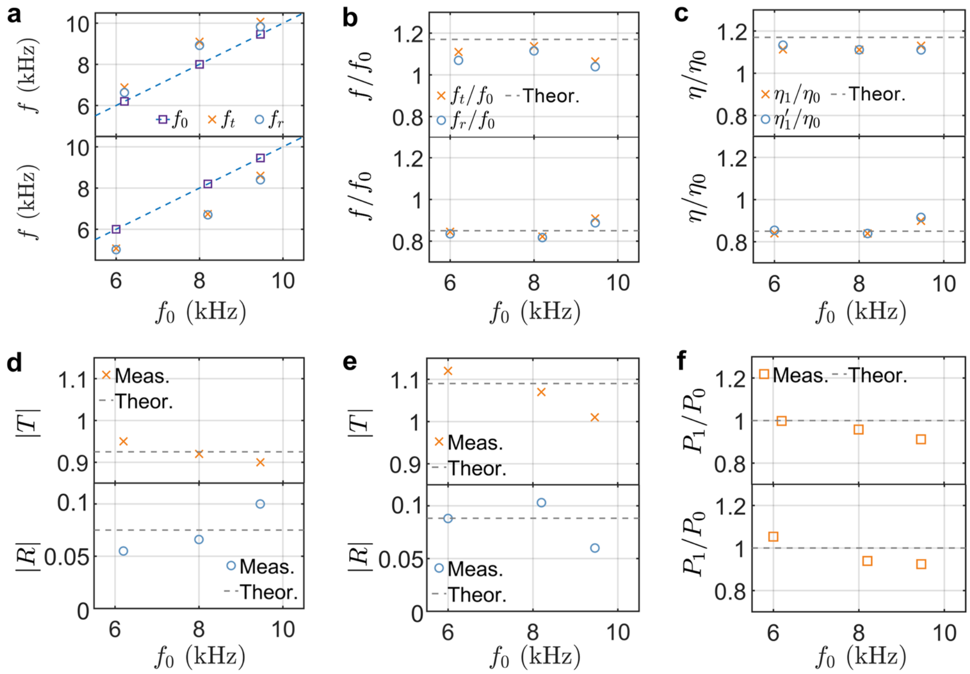

Fig. 3 | Verification of temporal Snell's law, Fresnel equations, and momentum conservation. **a** The measured frequencies of the incident (squares) and reflected (circles) signals at $x/L = 0.05$, and the refracted signal (crosses) observed at $x/L = 1$, plotted against the incident frequency f_0. The top (bottom) panel represents the results for the switch from ON to OFF (from OFF to ON). **b** Normalized frequencies of the refracted and reflected waves, along with the theoretical prediction of Snell's law (dashed line). The top (bottom) panel represents the results for the switch from ON to OFF (from OFF to ON). **c** The measured ratio of the tangent of the refraction angle ($\eta_1 = \tan\alpha_1$) to the tangent of the incidence angle ($\eta_0 = \tan\alpha_0$), along with the measured ratio of the tangent of the reflection angle ($\eta'_1 = \tan\alpha'_1$) to the tangent of the incidence angle, is compared with the theoretical prediction based on Snell's law (represented by the dashed line). The top (bottom) panel represents the results for the switch from ON to OFF (from OFF to ON). **d** The measured and theoretical magnitudes of the refraction coefficient (top panel) and reflection coefficient (bottom panel) at $t/t_f = 2/3$ for the switch from ON to OFF, plotted against the incident frequency f_0. **e** The measured and theoretical magnitudes of the refraction coefficient (top panel) and reflection coefficient (bottom panel) at $t/t_f = 2/3$ for the switch from OFF to ON, plotted against the incident frequency f_0. **f** The ratio of momentum before and after the temporal interface, along with the theoretical prediction based on momentum conservation (shown as the dashed line). The top panel shows the results for the switch from ON to OFF, while the bottom panel corresponds to the switch from OFF to ON.

also known as Noether's charge, of the elastic beam is given by

$$P = \int \rho A\left[(\partial_t w)^{\dagger}\partial_x w + \partial_t w(\partial_x w)^{\dagger}\right]dx, \tag{13}$$

where † denotes the Hermitian conjugate. The detailed derivation of Eq. (13) using the complex scalar field theory of the Euler-Bernoulli beam is provided in Supplementary Section 12. The momentum of the wave before the time switching is

$$P_0 = 2\rho A\omega_0 k_0 A_i^2, \tag{14}$$

whereas the momentum of the waves after the switching time is

$$P_1 = 2\rho A\omega_1 k_0 (T^2 - R^2)A_i^2. \tag{15}$$

With the aid of Eq. (9), the conservation of momentum can be easily verified as

$$P_0 = P_1 = 2Z_0 k_0^3 A_i^2. \tag{16}$$

In addition, the momentum of both the incident and scattered waves is proportional to k_0^3, indicating that the wavenumber remains invariant. It is worth noting that although the full electromechanical system conserves energy, our analysis treats the mechanical beam as an open subsystem. The shunting circuit serves as an engineered environment that modulates stiffness, resulting in mechanical energy exchange and thus energy non-conservation, while momentum remains conserved through spatial translation symmetry.

Guided by the derived Snell's law in Eq. (7), the frequency conversion capability for different incident frequencies at the temporal interface is further tested experimentally. Figure 3a presents the measured central frequencies of the refracted (crosses) and reflected (circles) waves at the temporal interface as a function of the incident frequency f_0 (squares), for both the switch from ON to OFF (top panel) and OFF to ON (bottom panel). In the figure, the corresponding time-domain signals are measured at $x/L = 0.05$ for the incident and reflected waves, and at $x/L = 1$ for the refracted wave. The frequencies of the refracted and reflected waves shift upward (downward) during the transition from ON to OFF (OFF to ON), confirming the occurrence of frequency conversion. Furthermore, the frequencies of the refracted and reflected waves, normalized by the frequency of the incident wave, are presented in Fig. 3b. Additionally, Fig. 3c presents the tangents of the angles for the incident, refracted, and reflected waves, with the corresponding angles provided in Supplementary Table 3. The discrepancy observed for the switch from ON to OFF at 6 kHz arises because low-frequency incident signals do not terminate before reaching the temporal boundary, while the discrepancy at high frequencies is attributed to the limitations of the homogeneous beam model at short wavelengths. Therefore, the 6–10 kHz range is deliberately selected to balance the wavelength considerations and maintain the validity of the continuum beam model. Overall, these normalized frequencies and tangent ratios agree with the theoretical predictions ($n_0/n_1 = 1.17$ in the top panel and $n_0/n_1 = 0.85$ in the bottom panel) derived from Snell's law in Eq. (7) and Eq. (8). This agreement confirms that the observed frequency conversion and directional changes are consistent with the analytical predictions based on the temporal analog of Snell's law.

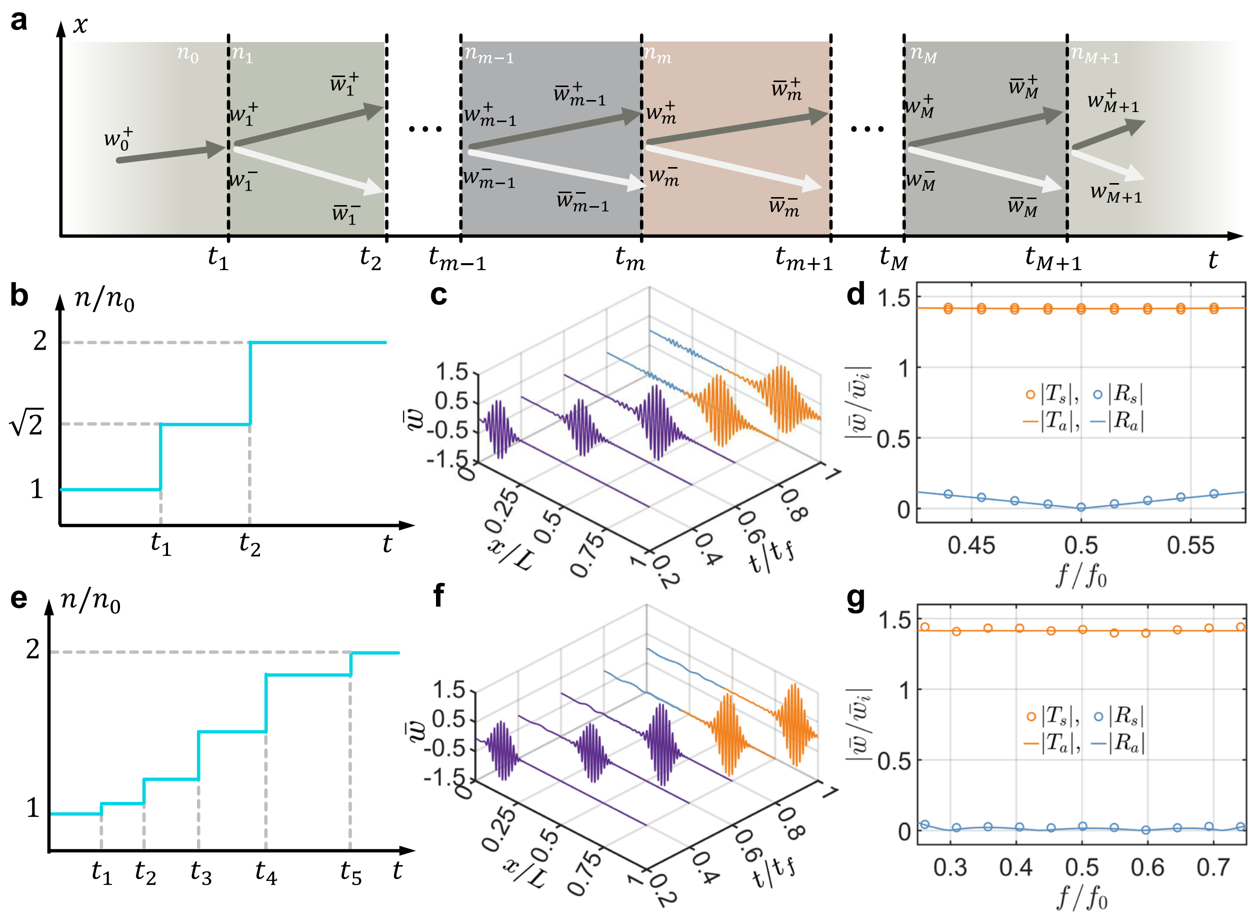

Fig. 4 | Multi-stepped temporal interfaces for anti-reflection. a Schematic diagram illustrating a wave propagating through multi-stepped temporal interfaces. The setup consists of two temporally semi-infinite media with a cascade of M temporal slabs, separated by $M+1$ temporal interfaces. **b**, **e** The optimal time-dependent index of refraction function designed for anti-reflection of a single frequency (**b**) and broadband frequency (**e**). **c**, **f** Wave packet evolution by COMSOL simulation for verifying anti-reflection of a single frequency (**c**) and broadband frequency (**f**). The wave packet, with a central frequency of 6 kHz, consists of 5 cycles in time, with $t_f = 6$ ms and $L = 2.56$ m. **d**, **g** Refraction and reflection coefficients as a function of the normalized incident frequency f/f_0 for single frequency (**d**) and broadband frequency (**g**) anti-elimination, where $f_0 = 6$ kHz, with circles representing numerical simulation results and solid lines representing analytical calculations using the transfer matrix method. The subscripts "s" and "a" denote simulated and analytical results, respectively. The results are obtained from the Fourier transform at $t/t_f = 0.75$ in (**c**) and (**f**).

The derived Fresnel equations in Eq. (9) across the temporal boundary are also verified. The amplitudes of the incident, refracted, and reflected waves are defined as the height of spectral peaks, as shown in Fig. 2h. The corresponding spatial-domain signals are measured at $t/t_f = 1/3$ for the incident wave, and at $t/t_f = 2/3$ for the refracted and reflected waves. Figure 3d, e show the measured amplitudes of the refraction coefficient (T, crosses), reflection coefficient (R, circles), and their theoretical predictions (dashed lines) based on Eq. (9), as functions of the incident frequency for the switches from ON to OFF and OFF to ON, respectively. In Fig. 3d, the measured amplitudes closely match the theoretical predictions of $|T| = 0.925$ and $|R| = 0.075$ for the switch from ON to OFF at the given incident frequencies. Similarly, the minor deviation between the experimental measurement and theoretical predictions may be attributed to the absence of the low-frequency incident signals and the limitations of the homogeneous beam model. Also, as shown in Fig. 3e, the measured amplitudes are mainly consistent with the theoretical predictions of $|T| = 1.09$ and $|R| = 0.089$ for switching OFF to ON at different incident frequencies. A small deviation is also observed. However, the reasonable consistency verifies the elastic analog of the Fresnel equations across various incident frequencies. Finally, the ratio of momentum before and after the temporal interface is presented in Fig. 3f. The momentum ratios are mainly close to 1 for both the switch from ON to OFF and from OFF to ON, validating momentum conservation.

Flexural wave engineering with temporal multi-stepped interfaces

Leveraging scattering phenomena at a single temporal interface, we explore the engineering of flexural wave interferences in time, inspired by their photonic counterparts, such as in discrete temporal crystals and temporal metabeams analogous to the optical counterpart[24,60,61]. To demonstrate this, we consider flexural wave propagation through a temporal modulation of the bending stiffness characterized by $M+1$ stepped temporal interfaces, as depicted in Fig. 4a. The unbounded medium initially has a refractive index n_0 for times $t < t_1$. At $t = t_1$, a temporal modulation of the refractive index occurs, characterized by n_m, $m = 1, 2, \ldots, M$ over M intervals. This assumption of step temporal transitions is highly idealized, as it implies an infinitely fast response of the medium to the modulation. The theory of wave propagation through multi-stepped temporal interfaces in an unbounded medium is developed using the rigorous transfer matrix approach. The wave components on the left and right sides of the mth temporal slab are represented by $[w_m^+, w_m^-]^{\mathrm{T}}$ and $[\tilde{w}_m^+, \tilde{w}_m^-]^{\mathrm{T}}$, respectively. These components are connected by the following expression:

$$\begin{bmatrix} \tilde{w}_m^+ \\ \tilde{w}_m^- \end{bmatrix} = \mathbf{N}_a^m \begin{bmatrix} w_m^+ \\ w_m^- \end{bmatrix}, \tag{17}$$

where the propagation matrix $\mathbf{N}_a^m$ is

$$\mathbf{N}_a^m = \begin{bmatrix} e^{-i\omega_m \Delta t_m} & 0 \\ 0 & e^{i\omega_m \Delta t_m} \end{bmatrix}, \tag{18}$$

and the mth time interval is $\Delta t_m = t_{m+1} - t_m$. In addition, due to the continuity equations in Eq. (2), the wave components $[w_m^+, w_m^-]^{\mathrm{T}}$ and $[\tilde{w}_{m-1}^+, \tilde{w}_{m-1}^-]^{\mathrm{T}}$ on either side of mth temporal interface satisfy the following relation:

$$\begin{bmatrix} w_m^+ \\ w_m^- \end{bmatrix} = \mathbf{N}_b^m \begin{bmatrix} \tilde{w}_{m-1}^+ \\ \tilde{w}_{m-1}^- \end{bmatrix}. \tag{19}$$

Here, the matching matrix $\mathbf{N}_b^m$ is

$$\mathbf{N}_b^m = \begin{bmatrix} T_m & R_m \\ R_m & T_m \end{bmatrix}. \tag{20}$$

where $T_m = 1 + Z_{m-1}/Z_m$ and $R_m = 1 - Z_{m-1}/Z_m$. Applying Eqs. (17) and (19) recurrently, we obtain the relationship between the waves in the initial and final temporal boundaries:

$$\begin{bmatrix} w_{M+1}^+ \\ w_{M+1}^- \end{bmatrix} = \mathbf{N} \begin{bmatrix} w_0^+ \\ 0 \end{bmatrix}, \tag{21}$$

where the overall transfer matrix $\mathbf{N}$ is given as follows:

$$\mathbf{N}(\boldsymbol{n}, \boldsymbol{t}, f_0) = \mathbf{N}_b^{M+1} \prod\nolimits_{m=1}^{M} \mathbf{N}_a^m \mathbf{N}_b^m. \tag{22}$$

Here, $\boldsymbol{n}$ and $\boldsymbol{t}$ are vectors representing the refractive indices n_m (for $m = 1, 2, \ldots, M$) and the times at different interfaces t_m (for $m = 1, 2, \ldots, M+1$), respectively. f_0 denotes the wave frequency in the left unbounded medium. Additionally, the refraction coefficient is defined as $T(\boldsymbol{n}, \boldsymbol{t}, f_0) = w_{M+1}^+ / w_0^+ = N_{11}$, and the reflection coefficient is defined as $R(\boldsymbol{n}, \boldsymbol{t}, f_0) = w_{M+1}^- / w_0^+ = N_{21}$.

Using the analytical solutions for the reflection and refraction coefficients, we will explore three examples of engineered flexural wave propagation across multi-stepped temporal interfaces through inverse design. These examples will leverage temporal intervals and modulated slab parameters, demonstrating the potential of temporal multi-stepped interfaces as versatile wave transformers. First, we investigate anti-reflection temporal coatings by introducing two-stepped temporal slabs with equal travel times to achieve impedance matching and frequency conversion between two connected waveguides with different stiffnesses, analogous to quarter-wavelength impedance matching in the spatial domain[62]. Second, we employ multi-stepped temporal interfaces composed of five temporal slabs to achieve broadband wave anti-reflection[60]. Finally, we propose temporal multi-stepped interfaces with alternating high and low refractive indices to enable wave amplification in both reflection and refraction[61]. The temporal parameters of these multi-stepped structures are determined using an optimization method, which seeks to identify the optimal temporal interface parameters by minimizing a target function related to the reflection and refraction coefficients, subject to specified constraints. Detailed formulations of the optimization problem for the three cases are provided in Supplementary Section 13, and the optimized results will be validated against the analytical solution from Eq. (22) for multi-stepped interfaces using the optimized parameters.

Figure 4b presents the numerically derived two-stepped temporal configuration, consisting of a single temporal slab with a refractive index n_1, designed to eliminate the reflection of an incident flexural wave at a frequency of $f_0 = 6$ kHz, closely matching our experimental testing conditions. The duration of the temporal slab is defined as $\Delta t_1 = t_2 - t_1$. The wave initially propagates through a medium with a refractive index of n_0, while the final medium has a refractive index of $n_2 = 2n_0$. By minimizing the square of the reflection coefficient magnitude at the frequency (see Supplementary Section 13 for details), we obtain the optimal values of $n_1 = 1.414n_0$ and $\Delta t_1 = 0.3536/f_0$. These results are in excellent agreement with the analytical solution in Eq. (21), where $n_1 = \sqrt{2}n_0$ and $t_2 = 1/(2\sqrt{2}f_0)$ (see Methods)[24]. Since the time duration t_2 equals a quarter of the wave period in the slab, this temporal medium is referred to as a quarter-wave transformer. Physically, as the incident wave passes through two temporal interfaces, it generates two refracted and two reflected waves. In the quarter-wave transformer, the two reflected waves cancel each other through coherent subtraction. Using the optimized parameters, Fig. 4c illustrates the evolution of a wave packet with a central frequency of $f_0 = 6$ kHz as it propagates through the temporal quarter-wave transformer. The simulation is performed in a long temporal metabeam with 240 unit cells (see Supplementary Section 4 for details on refraction and reflection without the temporal slab). In Fig. 4c, the reflected wave packet is almost entirely suppressed, though two small wave packets with different frequencies are generated. This occurs because the transformer perfectly eliminates reflection at the frequency, while residual components remain at other frequencies[24]. Additional simulations were performed for wave packets with different central frequencies, and the corresponding refraction coefficient T_s and reflection coefficient R_s are plotted in Fig. 4d. In this figure, the numerical refraction coefficient T_s and reflection coefficient R_s (circles) closely match the analytical refraction coefficient T_a and reflection coefficient R_a (solid lines), calculated using the transfer matrix method. The reflection coefficient approaches zero near $0.5f_0$ but diverges significantly at other frequencies, confirming that the temporal quarter-wave transformer eliminates reflection optimally and shifts the frequency component to the frequency $0.5f_0$. The magnitude of the frequency shift is determined by the refractive index change through the temporal interfaces. It is also observed that the values of scattering coefficient T_s are greater than unity for most frequencies, revealing a gain effect induced on the propagating signal by the medium, where energy conservation is violated.

To achieve broadband wave anti-reflection, the multi-stepped interfaces are determined using an optimization method. Figure 4e shows the resulting temporal medium with four slabs, characterized by $\boldsymbol{n} = [1.075, 1.271, 1.573, 1.860]n_0$ and $\boldsymbol{t} = [0, 0.262, 0.575, 0.962, 1.416]/f_0$, designed for broadband anti-reflection across the frequency range from $0.5f_0$ to $1.5f_0$. The initial and final refractive indices are n_0 and $n_2 = 2n_0$, respectively. These parameters are derived by minimizing the integral of the squared reflection coefficient over the same frequency range (see Supplementary Section 13 for details). The wave packet evolution in this medium is shown in Fig. 4f, where reflections are significantly suppressed, except for minor low- and high-frequency noise. Figure 4g shows the simulated and analytical refraction and reflection coefficients in the frequency domain, with the simulated reflection coefficient staying near zero across the range from $0.25f_0$ to $0.75f_0$, where the frequency shifts relative to the incident frequency. This result is consistent with the analytical results from the transfer matrix method, confirming the accuracy of the optimization method and the effectiveness of temporal multi-stepped interfaces for broadband anti-reflection.

Different from spatial interfaces, time interfaces can provide energy to the input waves; hence, through interference, it is possible to design time scattering profiles that achieve broadband wave amplification in both reflected and refracted waves. Figure 5a presents optimal parameters to achieve this task for a temporal multilayer with three slabs, where $\boldsymbol{n} = [3, 1, 3]n_0$ represents the refractive indices and $\boldsymbol{t} = [0, 0.75, 0.25, 0.75]/f_0$ represents the corresponding time intervals. The initial refractive index is denoted by n_0. These parameters are obtained by minimizing the negative square of the magnitude of the refraction coefficient at 6 kHz (see Supplementary Section 13 for details). The length of each slab is a quarter of the wave period, resulting in a phase decrease of $\pi/4$ for the refracted wave and a phase increase of $\pi/4$ for the reflected wave. After passing through each slab, the phase difference between the refracted and reflected waves reaches π, leading to constructive interference at the subsequent temporal interface, which amplifies the waves[30]. The wave packet evolution in this medium is shown in Fig. 5b, where significant amplification of both refraction and reflection is observed. Figure 5c shows that the simulated reflection coefficient peaks at ~4.5 around the frequency f_0, closely matching the analytical results from the transfer matrix method. Although the refraction coefficient is optimized for a specific frequency, amplification is observed over a broad frequency range, spanning from $0.6f_0$ to $1.4f_0$.

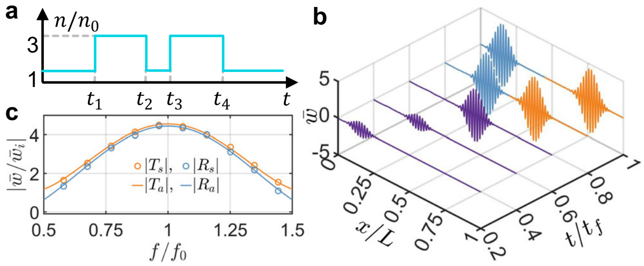

Fig. 5 | Multi-stepped temporal interfaces for wave amplification. a The optimal distribution of the index of refraction with 4 temporal interfaces for wave amplification. **b** The evolution of the wave packet is simulated using COMSOL to verify wave amplification. This wave packet, with a central frequency of 6 kHz, consists of 5 cycles for $t_f = 6$ ms and spans a length of $L = 2.56$ m. **c** Refraction and reflection coefficients as a function of the normalized incident frequency f/f_0, where $f_0 = 6$ kHz, with circles representing numerical simulation results and solid lines representing analytical calculations using the transfer matrix method. The subscripts "s" and "a" denote simulated and analytical results, respectively. The results are obtained from the Fourier transform of data at $t/t_f = 0.75$ in (**b**).

Temporal metabeams for smart waveform morphing and information coding

In this section, we propose a method for designing temporal metabeams with tunable time-varying bending stiffness by utilizing self-reconfigurable transfer functions controlled by time-varying digital potentiometers. By programming the time-domain behavior of these digital potentiometers, the metabeam's bending stiffness can be modulated to follow desired periodic or aperiodic patterns. The proposed time-varying metabeam demonstrates capabilities in shaping the amplitudes of transmitted flexural waves in the time domain, both experimentally and numerically, as illustrated in Fig. 6a. It is essential to emphasize that the time-varying parameters must meet adiabatic conditions, meaning the bending stiffness should change gradually enough to avoid inducing frequency conversion at the temporal stepped interface.

Under the assumption of the length of the unit cell being much shorter than the wavelength, the effective bending stiffness of the metabeams could be positive and negative. Previous studies employed metabeams with time-varying negative bending stiffness to modulate the amplitude of flexural waves within the subwavelength Bragg bandgap[59,63]. For the metabeam with the negative stiffness, the flexural wave will exponentially decay in a factor proportional to the magnitude of the effective bending stiffness (see Supplementary Section 1). Therefore, the negative stiffness of the metabeam with temporal variability spanning a reasonable range could result in a significant change in wave transmission. The time-varying bending stiffnesses are difficult to measure directly; hence, we indirectly verify their existence by studying the wave transmission properties of the metabeam. To understand the underlying mechanism of this method, we analyze the influences of the constitutive parameters on the wave transmission of a metabeam with 30 unit cells.

A time-varying transfer function is applied to the metabeam to achieve the desired waveform morphing. For instance, the transfer function can be modulated as a sinusoidal or smooth step function

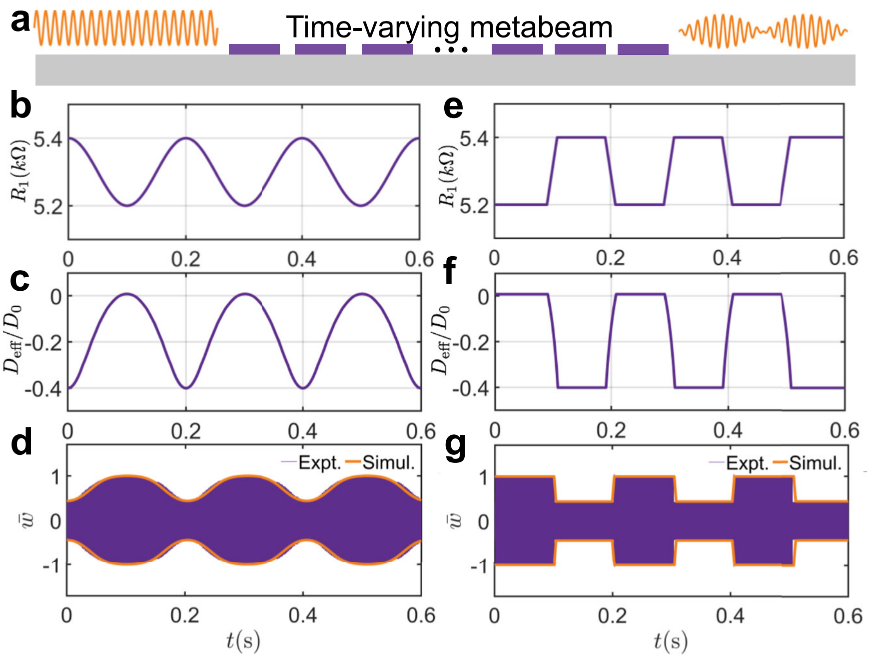

Fig. 6 | Smart waveform morphing schematic enabled by a smooth time-varying metabeam. a Schematic illustration of smart waveform morphing enabled by a time-varying metabeam. **b**, **e** The transfer function can be modulated into various forms, such as a sinusoidal function (**b**) and smooth step function (**e**). **c**, **f** The corresponding effective bending stiffness over time at frequencies of 33 kHz of sinusoidal function and smooth step function, respectively. **d**, **g** The simulated response (encapsulated by an orange envelope) and the measured time response (purple lines) at a point on the right side of the beam of the sinusoidal function and smooth step function, respectively. The excitation source, with a frequency of 33 kHz, is located at the leftmost piezoelectric patch.

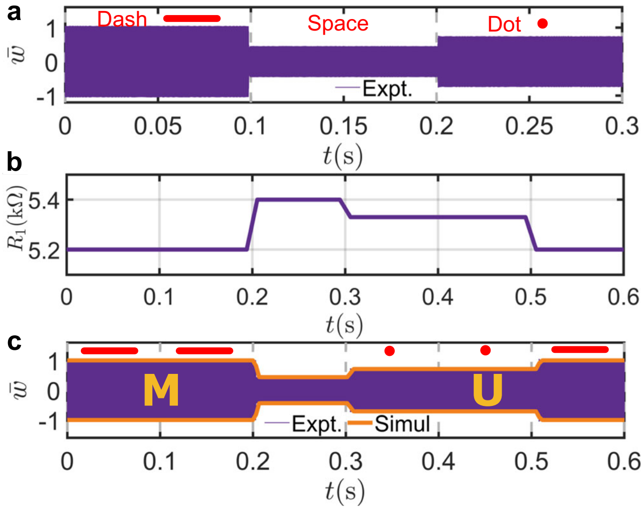

Fig. 7 | Time-varying metabeam for Morse coding. a Experimental demonstration of the fundamental Morse code elements—dash, space, and do—using flexural waves with distinct amplitude levels. The experimental variation remains within ±2.5%; the amplitude difference between a dash and a dot exceeds 30%, while that between a space and a dot is ~15%. **b** Time profile of the resistance $R_1(t)$, used to modulate the beam's effective stiffness to generate these signals. **c** Comparison of experimental (purple) and simulated (orange) signals encoding the text "MU".

using a time-varying digital potentiometer, as shown in Fig. 6b, e. For an excitation frequency of 33 kHz, the corresponding effective bending stiffness over time is plotted in Fig. 6c, f. An excitation frequency of 33 kHz is chosen because it corresponds to the transition of the effective bending stiffness from positive to negative values under circuit tuning. The detailed smooth functions can be found in Supplementary Section 14. The results in Fig. 6c, f show that the modulation pattern of the bending stiffness can be flexibly tuned to any desired shape by programming the transfer functions. Next, we demonstrate that modulating the constitutive parameters can be used for waveform morphing. Using sinusoidal and smooth step function patterns as examples, we measure the transmitted waves for different modulation amplitudes, as shown in Fig. 6d, g. As shown in Fig. 6d, g, the variations in bending stiffness are clearly reflected in the changing amplitudes of the transmitted wave, demonstrating that the metabeam can modulate the amplitude of transmitted signals in a desired periodic manner. The experimental and simulated transmitted wave amplitudes are in excellent agreement, following the patterns predicted by the homogenized model. This confirms that the adiabatic assumption is satisfied, allowing the metabeam to be treated as a temporal Cauchy-elastic medium with strongly time-modulated constitutive parameters.

As an additional example, we utilize the metabeam as an elastic Morse coder to demonstrate its capability to modulate wave amplitudes in an aperiodic manner. Morse codes represent letters of the alphabet, numerals, and punctuation marks by arranging dots, dashes, and spaces, as depicted in Fig. 7a. Traditionally, the codes are transmitted as electric pulse, mechanical, or visual signals. Here, we program the codes with time-varying bending stiffness of the metabeam. These codes are distinguished by the amplitudes of the transmitted waves when the metabeam is excited on the left side by a constant sine signal at 33 kHz. Specifically, a "dash" is represented by the measured transmitted wave with the largest amplitude among the three states, and it is normalized to unit 1, as shown in Fig. 7a; a dot is represented by the normalized amplitude of the transmitted wave being 0.75; a space between letters is represented by the amplitude of the transmitted wave being 0.45. In addition, each state is designed to last 0.1 seconds in the time domain.

Using the coding rules, we encode "MU", the abbreviation for the University of Missouri, into the metabeam via a time-varying transfer function. The time-varying digital potentiometer corresponding to this transfer function is shown in Fig. 7b. The encoded information can be extracted by mechanically stimulating the left side of the metabeam with a constant 33 kHz sine signal and measuring the transmitted wave on the right side. The measured signal, shown in Fig. 7c, successfully transmits the letters "MU". The measured signals are in excellent agreement with our numerical simulations.

Discussion

This study presents the experimental observation of temporal refraction and reflection of flexural waves in a time-varying metabeam with time-modulated bending stiffness. We also demonstrated stepped and smooth variations of multiple time interfaces for enhanced wave control based on time scattering. Our metabeam, composed of an elastic beam with attached piezoelectric patches, is a mechanical platform well-suited to explore a wide range of time-varying media in ultrafast wave control and advanced signal processing technologies through time-varying transfer functions. The temporal variation patterns can be of periodic or non-periodic form, allowing for fast and flexible adjustment, and can even be controlled wirelessly. We have established analogs to Snell's law and Fresnel equations for elastic waves, providing a theoretical framework for understanding wave scattering at temporal boundaries, which was validated through experimental testing. Due to spatial translational symmetry, we show that momentum remains conserved, revealing the fundamental principles governing wave scattering in time-varying media. The rapid modulation of stiffness via elastic elements is scalable, and it can be applied to more complex designs, including damping compensation. A smooth time-varying metabeam was then implemented in waveguides, achieving anti-reflection temporal coatings, wave morphing, impedance matching, and efficient frequency conversion. Beyond these remarkable functionalities, the metabeam may serve as a platform to study phenomena like temporal pumping and k-space band gaps, inspiring the development of wave-based devices for signal processing.

Moving forward, this work opens exciting opportunities, in particular in the context of combining spatial and temporal interfaces for 4D elastic metamaterials[1]. Opportunities to realize elastic time crystals and quasi-crystals emerge in this platform, enabling the time analogs of sophisticated spatial wave features such as Hofstadter's butterfly and topological modes. Time-varying elastodynamic media introduce additional degrees of freedom for controlling and manipulating wave and material phases, expanding the design space for dynamic wave-based systems. The elastic wave platform introduced here offers interesting opportunities to explore these phenomena experimentally.

Methods

Sample fabrication

The metabeam is composed of 30 piezoelectric patches (APC 850: 10 mm × 10 mm × 0.8 mm) mounted via conductive epoxy onto the middle of an aluminum host beam (180 mm × 10 mm × 2 mm). In the circuit, the resistors $R_0 = 1\,\mathrm{M\Omega}$ and $R_2 = 10\,\mathrm{k\Omega}$ with 5% error, the capacitors are film capacitors with 5% error, the microcontroller is an STM32 Nucleo Development Board with an STM32F446RE MCU, the digital potentiometer R_1 is a 20 kΩ AD5291 from Analog Devices, and the analog switch is a DG411 from Vishay Siliconix.

Experimental procedures

In experiments, 30 piezoelectric patches are connected with control circuits, and another piezoelectric patch on their left is used to generate incident flexural waves. We employ three cycles of tone-burst signals with central frequencies at 6 kHz, 8 kHz, and 10 kHz for temporal refraction and reflection. We generate and amplify incident wave signals via an arbitrary waveform generator (Tektronix AFG3022C) and a high-voltage amplifier (Krohn-Hite), respectively. Transverse velocity wavefields are measured on the surface of the metamaterial by a scanning laser Doppler vibrometer (Polytec PSV-400). The analog switch is controlled by the microcontroller to turn off 0.3 ms after the reference signal, generated by the arbitrary waveform generator with an amplitude of 3 V, drops below −2V. For smart waveform morphing, the excitation is applied using a sinusoidal signal with a frequency of 33 kHz, and the velocity signal is measured at a position 0.2 m to the right of the rightmost piezoelectric patches.

Finite element simulations

The numerical simulations are conducted by using a 2D "Piezoelectricity, Solid" module in the commercial finite element software COMSOL Multiphysics. The material of the host beam is implemented by Aluminum [solid], and the material of the piezoelectric patches is PZT-5A from the COMSOL Material Library. The current passing through the top surface of the piezoelectric patch is coupled with voltage on the top surface by a transfer function using "Global ODEs and DAEs" module for simulating the circuit effect. The dispersion curves in Fig. 2h are obtained by using eigenfrequency analysis with Floquet boundary conditions. The time-domain analysis is conducted for the same setup as the experiment, where the transfer function is defined as a time-varying function. The simulations are performed using the generalized-α method, with a time step set to 1/100 of the wave period to accurately resolve the dynamic response. The boundary conditions on both sides for temporal refraction and reflection are free boundaries. However, two gradient-damping beams are attached on both sides to create perfect absorption boundary conditions for smart waveform morphing.

Temporal quarter-wave transformer

The temporal quarter-wave transformer comprises a slab with refractive index n_1 surrounded by two semi-infinite media with refractive indices n_0 and n_2, respectively. Therefore, the transfer matrix consists of two matching matrices and one propagation matrix combined as

$$\mathbf{N}=\begin{bmatrix} T_2 & R_2 \\ R_2 & T_2 \end{bmatrix}\begin{bmatrix} e^{-i\omega_1\Delta t_1} & 0 \\ 0 & e^{i\omega_1\Delta t_1} \end{bmatrix}\begin{bmatrix} T_1 & R_1 \\ R_1 & T_1 \end{bmatrix}. \tag{23}$$

Eq. (23) gives the reflection coefficient:

$$R=N_{21}=R_1T_2e^{i\omega_1\Delta t_1}+R_2T_1e^{-i\omega_1\Delta t_1}. \tag{24}$$

The reflection coefficient can be canceled out through coherent subtraction, which implies

$$R_1T_2e^{i\omega_1\Delta t_1}+R_2T_1e^{-i\omega_1\Delta t_1}=0. \tag{25}$$

This complex equation can be decomposed into two real equations corresponding to the amplitude and the phase:

$$\begin{aligned} \omega_1\Delta t_1 &= \frac{(2n+1)\pi}{2}, \\ R_2T_1 &= T_2R_1. \end{aligned} \tag{26}$$

These two equations give the anti-reflection conditions:

$$\begin{aligned} \Delta t_1 &= \frac{(2p+1)}{4f_1}, \\ n_1 &= \sqrt{n_0n_2}, \end{aligned} \tag{27}$$

where p is an integer, and f_1 is the wave frequency in the middle slab with refractive index n_1. If $p=0$, the slab length Δt_1 equals a quarter of the wave period, making this temporal medium a quarter-wave transformer. In the main text, with $n_2=2n_0$, we have $n_1=\sqrt{2}n_0$, $f_1=\sqrt{2}f_0/2$, and $t_2=1/(2\sqrt{2}f_0)$ for $p=0$ and $t_1=0$.

Data availability

The data supporting this study and its findings are available within the article and Supplementary Information. Data of this study are available from the corresponding author on request. Source data are provided with this paper.

Code availability

The codes that support the findings of this study are available from the corresponding author upon request.

References

1. Engheta, N. Four-dimensional optics using time-varying metamaterials. *Science* **379**, 1190–1191 (2023).
2. Galiffi, E. et al. Photonics of time-varying media. *Adv. Photonics* **4**, 014002–014002 (2022).
3. Yin, S., Galiffi, E. & Alù, A. Floquet metamaterials. *ELight* **2**, 1–13 (2022).
4. Zee, A. *Quantum field theory in a nutshell*, **7** (Princeton university press, 2010).
5. Ortega-Gomez, A., Lobet, M., Vázquez-Lozano, J. E. & Liberal, I. Tutorial on the conservation of momentum in photonic time-varying media. *Opt. Mater. Express* **13**, 1598–1608 (2023).
6. Miyamaru, F. et al. Ultrafast frequency-shift dynamics at temporal boundary induced by structural-dispersion switching of waveguides. *Phys. Rev. Lett.* **127**, 053902 (2021).
7. Lyubarov, M. et al. Amplified emission and lasing in photonic time crystals. *Science* **377**, 425–428 (2022).
8. Dikopoltsev, A. et al. Light emission by free electrons in photonic time-crystals. *Proc. Natl. Acad. Sci.* **119**, e2119705119 (2022).
9. Vázquez-Lozano, J. E. & Liberal, I. Incandescent temporal metamaterials. *Nat. Commun.* **14**, 4606 (2023).
10. Horsley, S. A. & Pendry, J. B. Quantum electrodynamics of time-varying gratings. *Proc. Natl. Acad. Sci.* **120**, e2302652120 (2023).
11. Koutserimpas, T. T. & Monticone, F. Time-varying media, dispersion, and the principle of causality. *Opt. Mater. Express* **14**, 1222–1236 (2024).
12. Li, H., Mekawy, A. & Alù, A. Beyond Chu's limit with Floquet impedance matching. *Phys. Rev. Lett.* **123**, 164102 (2019).
13. Hayran, Z. & Monticone, F. Beyond the Rozanov bound on electromagnetic absorption via periodic temporal modulations. *Phys. Rev. Appl.* **21**, 044007 (2024).
14. Yang, X., Wen, E. & Sievenpiper, D. F. Broadband time-modulated absorber beyond the bode-fano limit for short pulses by energy trapping. *Phys. Rev. Appl.* **17**, 044003 (2022).
15. Akhmanov, S., Sukhorukov, A. & Chirkin, A. Nonstationary phenomena and space-time analogy in nonlinear optics. *Sov. Phys. JETP* **28**, 748–757 (1969).
16. Kolner, B. H. Space-time duality and the theory of temporal imaging. *IEEE J. Quantum Electron.* **30**, 1951–1963 (1994).
17. Lustig, E. et al. Photonic time-crystals-fundamental concepts. *Opt. Express* **31**, 9165–9170 (2023).
18. Morgenthaler, F. R. Velocity modulation of electromagnetic waves. *IRE Trans. Microw. theory Tech.* **6**, 167–172 (1958).
19. Moussa, H. et al. Observation of temporal reflection and broadband frequency translation at photonic time interfaces. *Nature Physics* **19**, 1–6 (2023).
20. Dong, Z. et al. Quantum time reflection and refraction of ultracold atoms. *Nat. Photonics* **18**, 68–73 (2024).
21. Jones, T. R., Kildishev, A. V., Segev, M. & Peroulis, D. Time-reflection of microwaves by a fast optically-controlled time-boundary. *Nat. Commun.* **15**, 6786 (2024).

22. Qin, C. et al. Observation of discrete-light temporal refraction by moving potentials with broken Galilean invariance. *Nat. Commun.* **15**, 5444 (2024).
23. Plansinis, B., Donaldson, W. & Agrawal, G. What is the temporal analog of reflection and refraction of optical beams? *Phys. Rev. Lett.* **115**, 183901 (2015).
24. Pacheco-Peña, V. & Engheta, N. Antireflection temporal coatings. *Optica* **7**, 323–331 (2020).
25. Pacheco-Peña, V. & Engheta, N. Temporal equivalent of the brewster angle. *Phys. Rev. B* **104**, 214308 (2021).
26. Ponomarenko, S. A., Zhang, J. & Agrawal, G. P. Goos-hänchen shift at a temporal boundary. *Phys. Rev. A* **106**, L061501 (2022).
27. Qin, C. et al. Temporal goos-hänchen shift in synthetic discrete-time heterolattices. *Phys. Rev. Lett.* **133**, 083802 (2024).
28. Bacot, V., Labousse, M., Eddi, A., Fink, M. & Fort, E. Time reversal and holography with spacetime transformations. *Nat. Phys.* **12**, 972–977 (2016).
29. Tirole, R. et al. Double-slit time diffraction at optical frequencies. *Nat. Phys.* **19**, 999–1002 (2023).
30. Galiffi, E. et al. Broadband coherent wave control through photonic collisions at time interfaces. *Nat. Phys.* **19**, 1703–1708 (2023).
31. Wilczek, F. Quantum time crystals. *Phys. Rev. Lett.* **109**, 160401 (2012).
32. Zaletel, M. P. et al. Colloquium: quantum and classical discrete time crystals. *Rev. Mod. Phys.* **95**, 031001 (2023).
33. Kongkhambut, P. et al. Observation of a continuous time crystal. *Science* **377**, 670–673 (2022).
34. Carminati, R., Chen, H., Pierrat, R. & Shapiro, B. Universal statistics of waves in a random time-varying medium. *Phys. Rev. Lett.* **127**, 094101 (2021).
35. Sharabi, Y., Lustig, E. & Segev, M. Disordered photonic time crystals. *Phys. Rev. Lett.* **126**, 163902 (2021).
36. Apffel, B., Wildeman, S., Eddi, A. & Fort, E. Experimental implementation of wave propagation in disordered time-varying media. *Phys. Rev. Lett.* **128**, 094503 (2022).
37. Trainiti, G. et al. Time-periodic stiffness modulation in elastic metamaterials for selective wave filtering: theory and experiment. *Phys. Rev. Lett.* **122**, 124301 (2019).
38. Lustig, E., Sharabi, Y. & Segev, M. Topological aspects of photonic time crystals. *Optica* **5**, 1390–1395 (2018).
39. Pan, Y., Cohen, M.-I. & Segev, M. Superluminal k-gap solitons in nonlinear photonic time crystals. *Phys. Rev. Lett.* **130**, 233801 (2023).
40. Chong, C., Kim, B., Wallace, E. & Daraio, C. Modulation instability and wavenumber bandgap breathers in a time layered phononic lattice. *Phys. Rev. Res.* **6**, 023045 (2024).
41. Galiffi, E., Yin, S. & Alú, A. Tapered photonic switching. *Nanophotonics* **11**, 3575–3581 (2022).
42. Pang, K. et al. Adiabatic frequency conversion using a time-varying epsilon-near-zero metasurface. *Nano Lett.* **21**, 5907–5913 (2021).
43. Khurgin, J. B. et al. Adiabatic frequency shifting in epsilon-near-zero materials: the role of group velocity. *Optica* **7**, 226–231 (2020).
44. Chen, H., Yao, L., Nassar, H. & Huang, G. Mechanical quantum hall effect in time-modulated elastic materials. *Phys. Rev. Appl.* **11**, 044029 (2019).
45. Wang, S. et al. Smart patterning for topological pumping of elastic surface waves. *Sci. Adv.* **9**, eadh4310 (2023).
46. Chen, Z.-G., Zhang, R.-Y., Chan, C. T. & Ma, G. Classical non-abelian braiding of acoustic modes. *Nat. Phys.* **18**, 179–184 (2022).
47. Yang, Y. et al. Non-abelian physics in light and sound. *Science* **383**, eadf9621 (2024).
48. Delory, A. et al. Elastic wave packets crossing a space-time interface. *Phys. Rev. Lett.* **133**, 267201 (2024).
49. Kim, B. L., Chong, C. & Daraio, C. Temporal refraction in an acoustic phononic lattice. *Phys. Rev. Lett.* **133**, 077201 (2024).
50. Liu, Z. et al. Inherent temporal metamaterials with unique time-varying stiffness and damping. *Adv. Sci.* **11**, 2404695 (2024).
51. Wu, Q., Qian, H., Chen, Y. & Huang, G. Dynamic phononic crystals with spatially and temporally modulated circuit networks. *Acta Mech. Sin.* **39**, 723007 (2023).
52. Chen, Y., Li, X., Scheibner, C., Vitelli, V. & Huang, G. Realization of active metamaterials with odd micropolar elasticity. *Nat. Commun.* **12**, 5935 (2021).
53. Wu, Q. et al. Active metamaterials for realizing odd mass density. *Proc. Natl. Acad. Sci.* **120**, e2209829120 (2023).
54. Chen, Y., Li, X., Hu, G., Haberman, M. R. & Huang, G. An active mechanical Willis meta-layer with asymmetric polarizabilities. *Nat. Commun.* **11**, 3681 (2020).
55. Wu, Q., Zhang, X., Shivashankar, P., Chen, Y. & Huang, G. Independent flexural wave frequency conversion by a linear active metalayer. *Phys. Rev. Lett.* **128**, 244301 (2022).
56. Xia, Y. et al. Experimental observation of temporal pumping in electromechanical waveguides. *Phys. Rev. Lett.* **126**, 095501 (2021).
57. Hagood, N. W. & Von Flotow, A. Damping of structural vibrations with piezoelectric materials and passive electrical networks. *J. Sound Vib.* **146**, 243–268 (1991).
58. Marconi, J. et al. Experimental observation of nonreciprocal band gaps in a space-time-modulated beam using a shunted piezoelectric array. *Phys. Rev. Appl.* **13**, 031001 (2020).
59. Chen, Y., Hu, G. & Huang, G. A hybrid elastic metamaterial with negative mass density and tunable bending stiffness. *J. Mech. Phys. Solids* **105**, 179–198 (2017).
60. Castaldi, G., Pacheco-Peña, V., Moccia, M., Engheta, N. & Galdi, V. Exploiting space-time duality in the synthesis of impedance transformers via temporal metamaterials. *Nanophotonics* **10**, 3687–3699 (2021).
61. Ramaccia, D., Alù, A., Toscano, A. & Bilotti, F. Temporal multilayer structures for designing higher-order transfer functions using time-varying metamaterials. *Appl. Phys. Lett.* **118**, 101901 (2021).
62. Collin, R. E. *Foundations for microwave engineering* (John Wiley & Sons, 2007).
63. Chen, Y., Zhu, R., Barnhart, M. V. & Huang, G. Enhanced flexural wave sensing by adaptive gradient-index metamaterials. *Sci. Rep.* **6**, 35048 (2016).

Acknowledgements

G.H. acknowledges the support of the Air Force Office of Scientific Research under Grant No. AF 9550-18-1-0342 and AF 9550-20-1-0279 with Program Manager Dr. Gregg Abate. A.A. is supported by the NSF Science and Technology Center ‘Frontiers of Sound’ and the Simons Foundation.

Author contributions

S.W., N.S. and H.Q. designed the metabeam with integrated circuits and conducted the simulations and measurements. S.W. and H.C. developed the theoretical framework, with contributions from Q.W., A.A. and G.H. S.W., J.C., A.A., H.D. and G.H. interpreted and presented the experimental data. S.W. and G.H. led the writing of the paper and the Supplementary Information, with input from all authors. The problem was conceived by S.W., A.A., and G.H., and the project was supervised by G.H.

Competing interests

The authors declare no competing interests.

Supplementary Information: Experimental Realization of Temporal Refraction and Reflection in Elastic Beams

Shaoyun Wang,[1, *] Nan Shao,[1, *] Hui Chen,[2] Jiaji Chen,[1] Honghua Qian,[1]
Qian Wu,[1] Huilin Duan,[3] Andrea Alù,[4, 5, †] and Guoliang Huang[3, ‡]
[1] *Department of Mechanical and Aerospace Engineering,*
University of Missouri, Columbia, MO 65211, USA
[2] *Center for Mechanics Plus under Extreme Environments,*
School of Mechanical Engineering and Mechanics, Ningbo University, Ningbo 315211, China
[3] *Department of Mechanics and Engineering Science,*
College of Engineering, Peking University, Beijing 100871, PR China
[4] *Photonics Initiative, Advanced Science Research Center,*
City University of New York, New York, NY, USA
[5] *Physics Program, Graduate Center, City University of New York, New York, NY, USA*

(Dated: October 28, 2025)

CONTENTS

---

[*] These two authors contributed equally.
[†] Corresponding author:aalu@cuny.edu
[‡] Corresponding author:
guohuang@pku.edu.cn

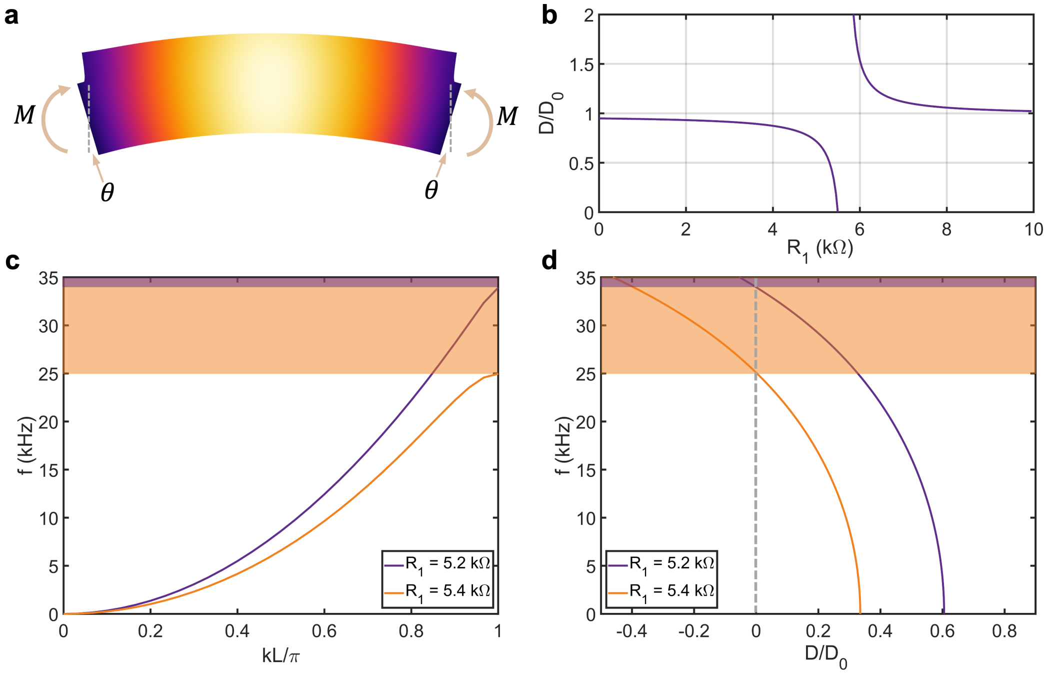

FIG. S1. **The effective bending stiffness and its application**. **a** Setup for determining the effective stiffness in the numerical test. **b** The relationship between normalized effective stiffness and R_1. D_0 represents the bending stiffness for the open circuit. **c** The dispersion curves for different values of R_1. The purple region indicates the bandgap for $R_1 = 5.2$ kΩ, while the orange region indicates the bandgap for $R_1 = 5.4$ kΩ. **d** The normalized stiffness as a function of frequency. The purple region shows the negative stiffness area for $R_1 = 5.2$ kΩ, and the orange region shows the negative stiffness area for $R_1 = 5.4$ kΩ.

1. DETERMINE THE EFFECTIVE BENDING STIFFNESS FROM NUMERICAL TESTS

A schematic diagram of the numerical test is shown in Fig. S1a. To determine the effective bending stiffness, the rotational angles at the left and right boundaries of the metabeam unit cell are set to $-\theta$ and θ, respectively, using rigid connectors in COMSOL. The vertical displacements at both boundaries are constrained to zero, while the horizontal displacements are left free. The reaction bending moment M at each rigid connector is obtained for calculating the effective bending stiffness. By solving the problem in the frequency domain, the effective bending stiffness D of the metabeam is defined following the approach described by Chen [**?**]:

$$D = \frac{M}{2\theta/L}, \tag{S1}$$

where L is the length of the unit cell. The normalized effective bending stiffness as a function of the resistor R_1 is shown in Fig. S1b. For R_1 values smaller than 5.5 kΩ, the normalized stiffness decreases to zero as R_1 increases, demonstrating the potential for tuning the bending stiffness using the negative capacitance circuit. For temporal refraction and reflection, $R_1 = 5$ kΩ, resulting in a normalized stiffness of $D/D_0 = 0.72$ at the operating frequency of 6 kHz, where $D_0 = 0.88\,\mathrm{N\cdot m^2}$. In general, the bending stiffness is frequency-dependent, and negative bending stiffness indicates the presence of bandgaps. As shown in Fig. S1c,d, the range of bandgaps corresponds to the range of negative normalized effective stiffness for different R_1 values. Additionally, the average density of the metabeam is $4143\,\mathrm{kg/m^3}$, and $\rho A = 0.116\,\mathrm{kg/m}$.

2. EXPERIMENTAL DETAILS

A. Geometric and material parameters of the metabeam

The metabeam consists of 30 unit cells, each equipped with a piezoelectric patch connected to a negative capacitance circuit via an analog switch, along with an additional unit cell used for excitation, as illustrated in Fig. S2a. The 30 piezoelectric patches are bonded to the aluminum beam using conductive epoxy, which is cured at room temperature for 24 hours. The spacing between adjacent piezoelectric patches is 0.67 mm. The geometric and material parameters of the metabeam, shown in Fig. S2b, are summarized in Table S1.

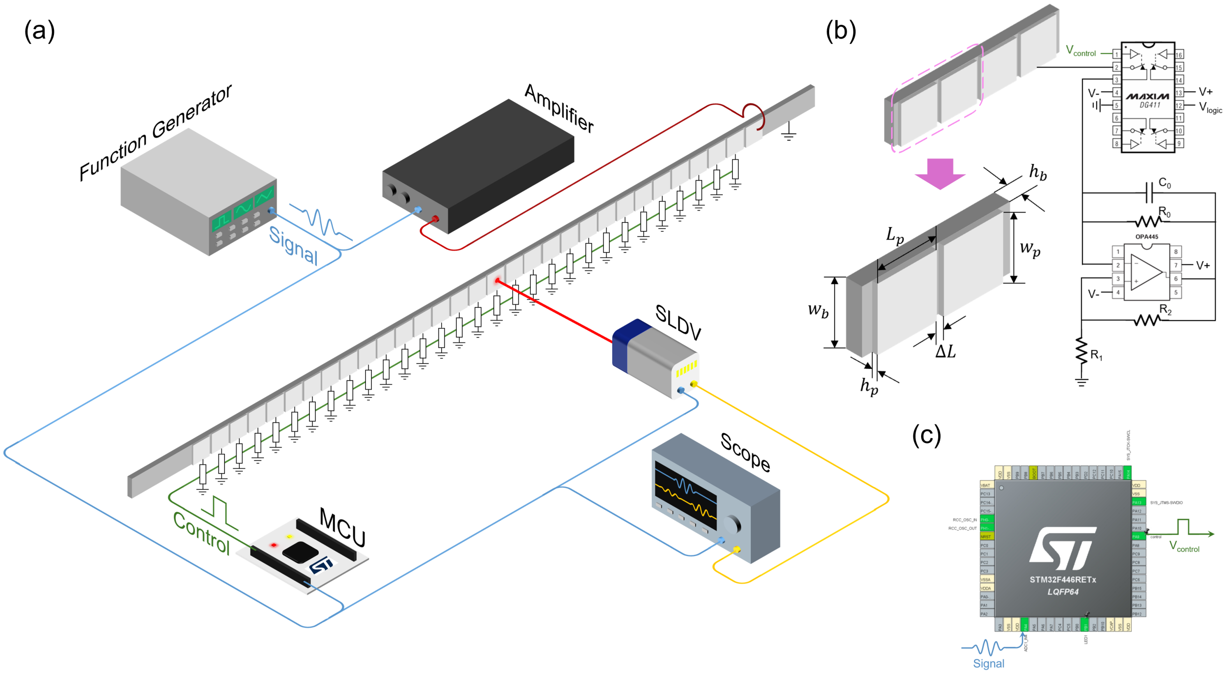

FIG. S2. **Practical experiment layout and measurement setup**. **a** Simplified schematic of the experimental setup. A signal generated by a function generator is amplified by a power amplifier to produce elastic waves through a piezoelectric patch. This signal also triggers an MCU to control all analog switches and activates the scanning laser Doppler vibrometer (SLDV) to measure the transverse velocity of the metabeam's surface. **b** Electrical control circuit layout and schematic for a single unit cell, along with its geometric parameters. **c** MCU pinout view.

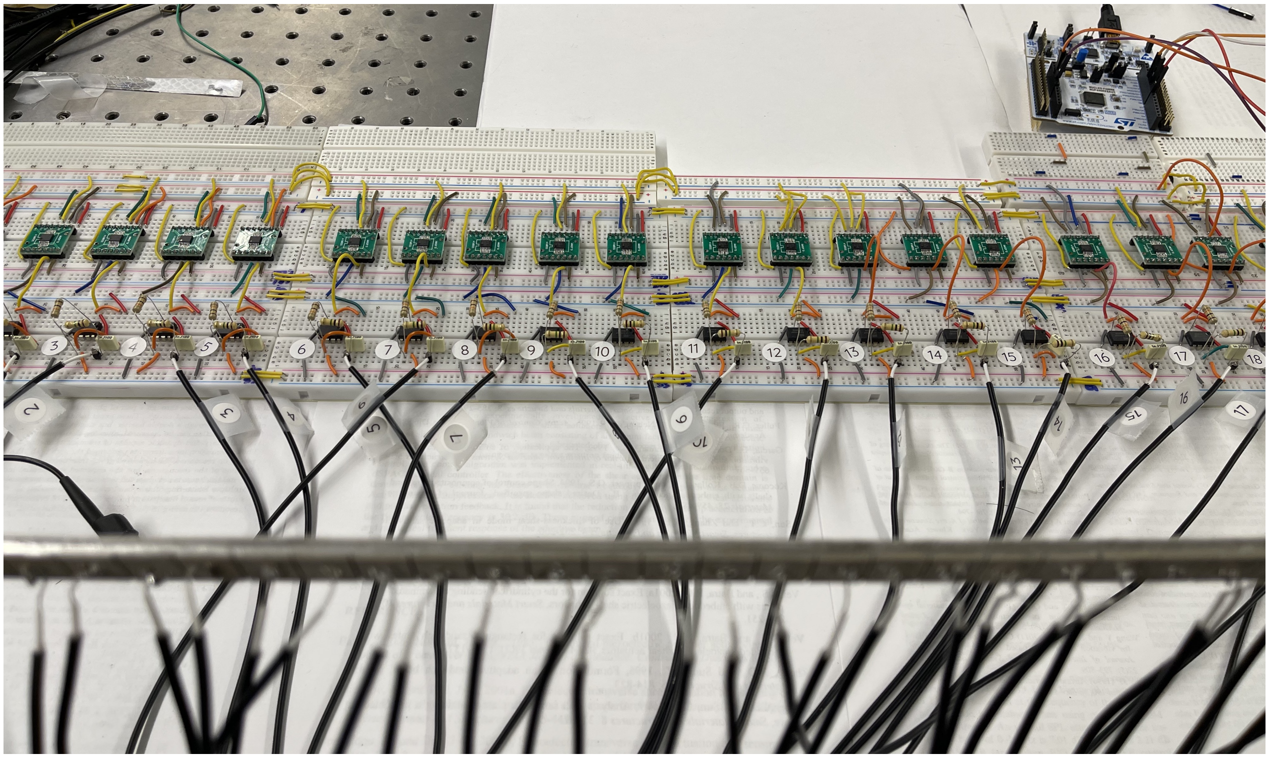

FIG. S3. **A photograph of metabeam with circuits**.

TABLE S1. **Geometric and material parameters of the metabeam**.

Parameter	Description	Value
h_b	Thickness of the host beam	2 mm
w_b	Width of the host beam	1 cm
L_p	Length of the piezoelectric patches	1 cm
h_p	Thickness of the piezoelectric patches	0.8 mm
w_p	Width of the piezoelectric patches	1 cm
ΔL	Interval between two piezoelectric patches	0.67 mm
E_b	Young's modulus of the aluminum beam	70 GPa
ρ_b	Density of the aluminum beam	2700 kg/m^3
s_{11}^E	Compliance matrix of the piezoelectric patches	1.64×10^{-11} 1/Pa
s_{33}^E	Compliance matrix of the piezoelectric patches	1.88×10^{-11} 1/Pa
s_{44}^E	Compliance matrix of the piezoelectric patches	4.75×10^{-11} 1/Pa
s_{66}^E	Compliance matrix of the piezoelectric patches	4.43×10^{-11} 1/Pa
s_{12}^E	Compliance matrix of the piezoelectric patches	-5.74×10^{-12} 1/Pa
s_{13}^E	Compliance matrix of the piezoelectric patches	-7.22×10^{-12} 1/Pa
d_{33}	Coupling matrix of the piezoelectric patches	3.74×10^{-11} C/N
d_{31}	Coupling matrix of the piezoelectric patches	-1.71×10^{-11} C/N
d_{15}	Coupling matrix of the piezoelectric patches	5.84×10^{-11} C/N
ϵ_{33}^S	Coupling matrix of the piezoelectric patches	$919.1\epsilon_0$
ϵ_{11}^S	Coupling matrix of the piezoelectric patches	$826.6\epsilon_0$
ϵ_0	Vacuum permittivity	8.842×10^{-12} F/m
ρ_p	Density of the piezoelectric patches	7750 kg/m^3

TABLE S2. **List of components used to fabricate metabeam, referred to the schematic shown in Fig. S2**.

Component	Description	Value
C_0	NC circuit capacitor	1 nF
R_0	NC circuit resistor	1 MΩ
R_1	NC circuit resistor	5 kΩ
R_2	NC circuit resistor	10 kΩ
Analog switch	DG411	
Operational amplifier	OPA445	
MCU	STM32F446	

B. Experiment layout and measurement setup

An electric signal generated by a function generator (Tektronix AFG3022C) is amplified by a power amplifier (Krohn-Hite) to excite elastic waves via the piezoelectric patch at rightmost. This signal simultaneously triggers a microcontroller unit (STM32F446RE) to control the analog switches and activates the scanning laser Doppler vibrometer (Polytec PSV-400) to measure the transverse velocity on the surface of the metabeam, as illustrated in Fig. S2a. A photograph of the

TABLE S3. **The angles of the incident wave, refracted wave, and reflected wave**.

Cases	α_0	α_1	α_1'
ON-to-OFF at 6 kHz	49.0°	52.0°	52.5°
ON-to-OFF at 6 kHz	48.0°	43.0°	43.5°
ON-to-OFF at 8 kHz	40.5°	43.5°	43.5°
OFF-to-ON at 8 kHz	45.0°	40.0°	40.0°
ON-to-OFF at 10 kHz	42.0°	45.5°	45.0°
OFF-to-ON at 10 kHz	42.0°	39.0°	39.5°

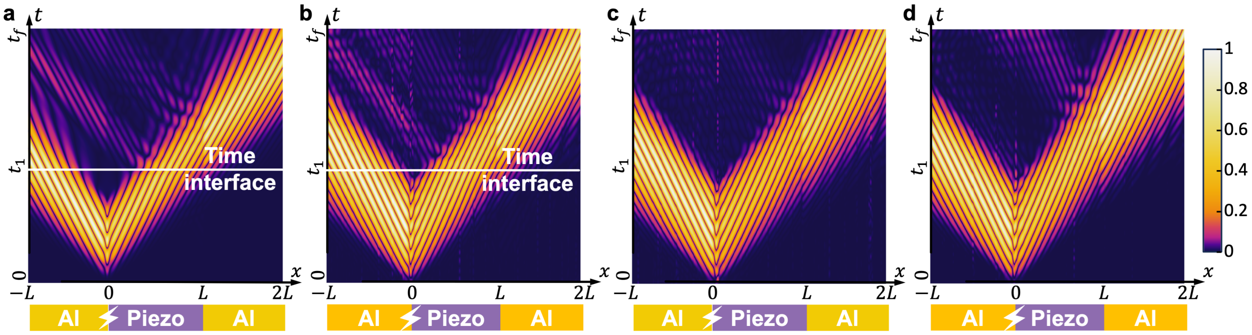

FIG. S4. **Spacetime diagram of temporal refraction and reflection without masks**. **a**, **b** The top panels show the simulation (**a**) and experimental results (**b**) of wave scattering from an incident wave packet consisting of 3 cycles in the time domain, with parameters $t_f = 1.1\,\mathrm{ms}$ and $t_1 = 0.44\,\mathrm{ms}$, at a time interface in a spacetime diagram. The bottom panels depict the system configuration, consisting of a length $L = 0.32\,\mathrm{m}$, composed of two aluminum beams (Al) and a piezo-metabeam (Piezo). The excitation source (indicated by the lightning symbol) is positioned at the left interface. **c**, **d** The spacetime diagrams illustrate the wave evolution with the switch permanently OFF (**c**) and permanently ON (**d**).

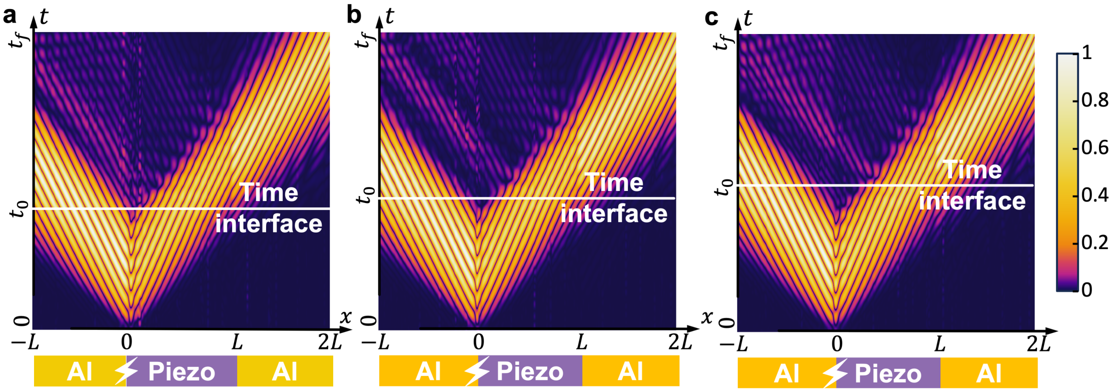

FIG. S5. **Temporal refraction and reflection at different switching times**. **a**, **b**, and **c** show the spacetime diagrams of wave evolution for switching times $t_1 = 0.435$ ms, $t_1 = 0.44$ ms, and $t_1 = 0.445$ ms, respectively.

experimental setup, showing the metabeam and its circuits, is presented in Fig. S3.

The laser Doppler vibrometer records data for 25.6 ms at a sampling rate of $f_s = 1.28$ MHz. The scanned domain, spanning 1.38 m, is discretized into a grid of 219 evenly spaced points, achieving a spatial resolution of 0.0063 m. Fig. S2b provides a schematic of the electrical control system used in each unit cell. The connection status between the piezoelectric patches and the negative capacitance circuits is controlled by analog switches, allowing adjustment of the effective stiffness of the metabeam. When V_{control} is at a high voltage level, the switch is OFF, and it is ON at a low voltage level. The switching time is less than 150 ns for transitions from OFF to ON and less than 100 ns for transitions from ON to OFF. These times are approximately 1000 times shorter than the bending wave period (about 150 µs), creating an ideal temporal interface.

All electrical circuits are constructed on solderless breadboards. The pinout of the MCU is shown in Fig. S2c. The MCU receives the reference signal through the analog-to-digital converter (ADC) at a sampling rate of 2 MHz. Once the voltage of the reference signal exceeds a specified threshold (−2 V), the MCU changes the state of the analog switch after a precisely programmed delay. The circuit parameters and components are detailed in Table S2.

3. VERIFICATION OF TEMPORAL REFLECTION IN THE EXPERIMENT

In Fig. 2a,c of the main text, masks were added to highlight the temporally reflected wave. Here, the masks are removed, and the original figures are presented in Fig. S4a,b. Since the behavior of spatially reflected waves, caused by spatial inhomogeneity, closely resembles that of temporally reflected waves, it is crucial to verify that the reflected waves in Fig. S4a,b are indeed temporally reflected waves rather than spatially reflected waves.

First, we perform a numerical simulation using the same setup as the experiment. The wave evolution in the spacetime diagram from the simulation is shown in Fig. S4a. Since the excitation is applied at the left interface between the aluminum beam and the piezoelectric metabeam, both a left-propagating wave and a right-propagating wave are generated. When the right-propagating wave reaches the right interface between the piezoelectric metabeam and the aluminum beam, a reflected wave is produced due to the spatial interface. In the simulation, an additional reflected wave is generated at the

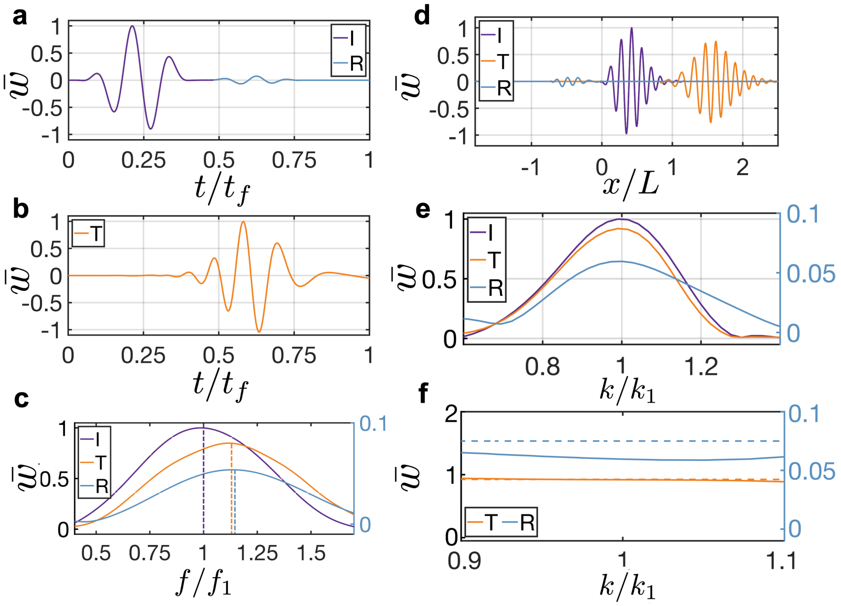

FIG. S6. **Spectral analysis of wave refraction and reflection at a time interface based on numerical simulation data**. **a** The incident (purple) and reflected (blue) signals measured at $x = 0.05L$. **b** The refracted signal (orange) observed at $x = L$. **c** Spectral analysis of the time-domain signals from (**a**, **b**). **d** The incident spatial profile (purple) measured at $t = 1/3t_f$, and the reflected and transmitted spatial profiles (blue and orange, respectively) measured at $t = 2/3t_f$. **e** Spectral analysis of the spatial-domain signals from (**d**). **f** The normalized spectral data for the incident, reflected, and refracted waves from (**e**), with each normalized by the amplitude distribution of the incident wave.

time interface, which is distinct from both the left-propagating wave caused by the excitation and the spatially reflected wave. This temporally reflected wave, also observed in the experiment (see Fig. S4b), closely resembles the one in the simulation, suggesting that it is indeed the time-reflected wave.

In the experiment, the piezoelectric metabeam consists of 30 unit cells, making it challenging to achieve perfect homogeneity across all cells. This inhomogeneity can potentially induce spatially reflected waves within the metabeam. To rule out this possibility, the spacetime diagrams of wave evolution with the switch permanently OFF and ON are presented in Fig. S4c,d for comparison. In these figures, no spatially reflected waves are observed in the middle of the metabeam, indicating that the metabeam is homogeneous. The homogeneity of the metabeam is ensured through the following steps. When the switch is OFF, homogeneity is maintained by carefully attaching the piezoelectric patches at constant intervals. When the switch is ON, resistors with $R_1 = 5$ kΩ are initially used, and the spacetime diagram is measured. While the metabeam is generally homogeneous, a few unit cells exhibit stiffness variations, leading to spatially reflected waves visible in the diagram. These abnormal cells are identified, and their resistors are replaced with potentiometers. By tuning the potentiometers until the reflected signals disappear from the PSV-400 screen, uniformity is achieved.

Furthermore, a key characteristic of a temporally reflected wave is that its position depends on the timing of the time interface. To verify this, we conduct three experimental tests with switching times of $t_1 = 0.435$ ms, 0.44 ms, and 0.445 ms, as shown in Fig. S5. In these figures, the position of the reflected wave shifts with changes in the time interface, confirming that the reflected wave depends on the time interface. This observation indicates that it is a temporally reflected wave rather than a spatially reflected one.

Based on these observations, we conclude that the reflected wave is a temporally reflected wave rather than a spatially reflected wave.

4. NUMERICAL SIMULATION OF TEMPORAL REFRACTION AND REFLECTION

A. Numerical simulation of temporal refraction and reflection in a metabeam

In Fig. 2(e–h), the temporal and spatial slices, along with their Fourier transforms, of the experimental spacetime diagram shown in Fig. 2(a) are presented. However, the corresponding results for the simulated spacetime diagram in Fig. 2(c) are not provided. Here, the corresponding simulation results are shown in Fig. S6 for comparison. The simulation results in Fig. S6 closely align with the experimental results in Fig. 3 of the main text. The frequency of the refracted and reflected waves is approximately 1.13 f_0, which is close to the theoretical value of 1.17 f_0. Furthermore, the normalized amplitude of the reflected wave with respect to the wave number is flatter and closely matches the theoretical prediction, indicating that the amplitude relation predicted in Eq. (9) of the main text holds over a wide frequency range.

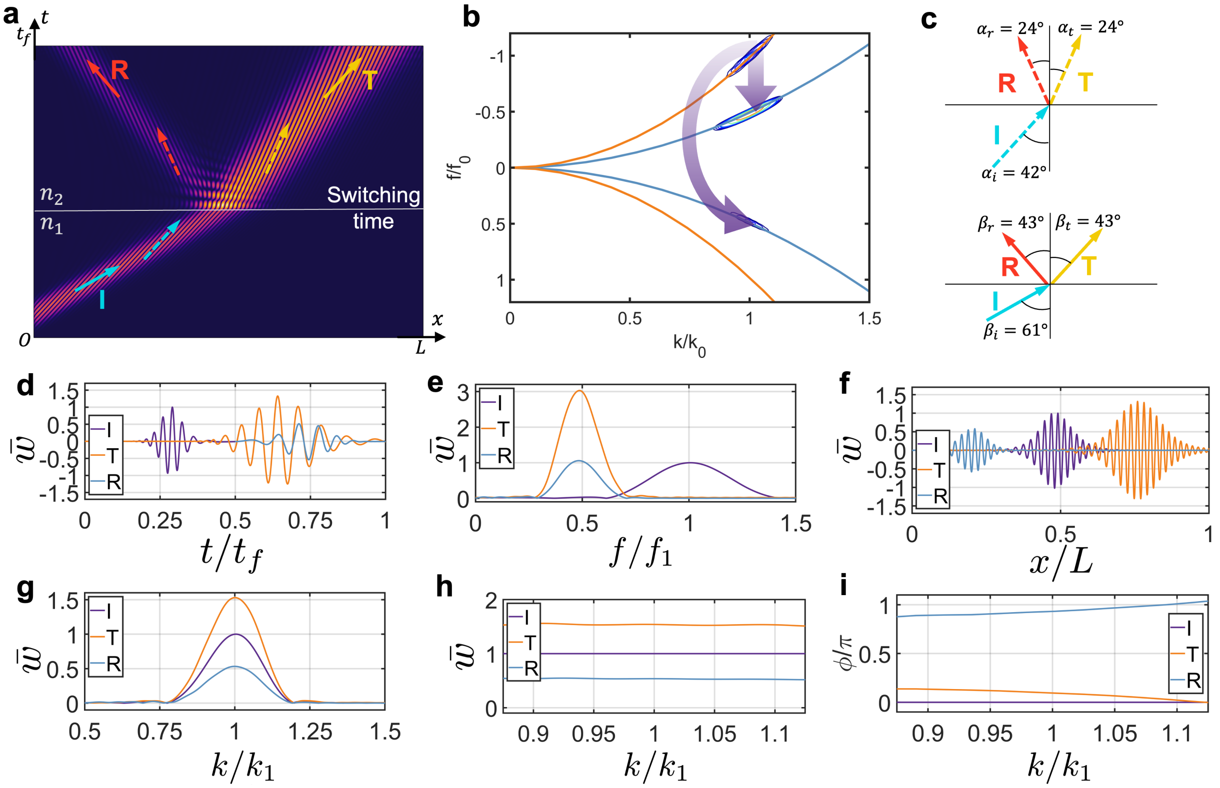

FIG. S7. **Numerical investigation of temporal refraction and reflection in a long metabeam.** **a** The refraction and reflection process of an incident wave packet, consisting of 5 cycles in the time domain, visualized in a spacetime diagram. Here, $L = 2.56\,\text{m}$ and $t_f = 6\,\text{ms}$. **b** The dispersion curves of the medium before (orange) and after (blue) the switching event, overlaid with a background contour diagram obtained from a 2D Fourier transform of the spacetime data in **a**. **c** The angular relationship between the incident, reflected, and refracted waves for both a plane wave and a wave packet, with arrows translated from the spacetime diagram in **a**. **d** The incident (purple) and reflected (blue) signals measured at $x = 0.28L$, and the refracted signal (orange) observed at $x = 0.62L$. **e** The spectral analysis of the time-domain signals in **d**. **f** The incident spatial profile (purple) measured at $t = 0.25t_f$, along with the reflected and transmitted spatial profiles (blue and orange, respectively) measured at $t = 0.75t_f$. **g** The spectral analysis of the spatial-domain signals in **f**. **h** The normalized spectral data for the incident, reflected, and refracted waves in **g**, each normalized by the amplitude distribution of the incident wave. **i** The relationship between phase and wavenumber.

B. Numerical simulation of temporal refraction and reflection in a long metabeam

In the experiment, the metabeam's normalized stiffness can be reduced to a minimum of 0.72, resulting in a relatively small reflected wave. To better observe temporal refraction and reflection, we perform a simulation using a long metabeam with 240 unit cells, excited by a 5-cycle tone burst. In the simulation, the switch transitions from OFF to ON, with the bending stiffness in the ON state being one-quarter of that in the OFF state. Under these conditions, the refractive index ratio is $n_1/n_0 = 2$, and the impedance ratio is $Z_1/Z_0 = 1/2$.

In Fig. S7a, the incident wave splits into a refracted wave and a reflected wave upon encountering the time interface. A 2D Fourier transform is applied to the data in Fig. S7a, with the results shown in Fig. S7b. In Fig. S7b, the frequency of the incident wave shifts from f_0 to $f_0/2$ and $-f_0/2$, while the wavenumber remains constant. In Fig. S7c, the directions of the incident, refracted, and reflected plane waves (solid arrows) and wave packets (dashed arrows) are derived from their respective components in Fig. S7a. The incident angle of the plane waves is $\alpha_i = 42°$, with refracted and reflected angles of $\alpha_t = 24°$ and $\alpha_r = 24°$, respectively. The ratio $\tan\alpha_t/\tan\alpha_i = 2.02$ closely matches the refractive index ratio $n_1/n_0 = 2$, verifying Snell's law in Eq. (S12) of the main text. For the wave packet, the incident angle is $\beta_i = 61°$, while the refracted and reflected angles are $\beta_t = 43°$ and $\beta_r = 43°$, respectively. The ratio $\tan\beta_t/\tan\beta_i = 1.93$ is close to the refractive index ratio, validating the geometric relationship of the wave packet described in Eq. (S13) of the main text.

Next, we validate the Fresnel equations presented in Eq. (9) of the main text. In Fig. S7d, the incident wave splits into a refracted wave and a reflected wave in the time domain. In the frequency domain, as shown in Fig. S7e, the frequencies of the refracted and reflected waves are approximately half that of the incident wave, quantitatively confirming the frequency shift after passing through the temporal interface, as described in Eq. (7) of the main text. In Fig. S7f, the incident wave splits into a refracted wave and a reflected wave in the spatial domain. The spectral data from Fig. S7f is presented in Fig. S7g. The wavenumbers of the waves remain constant, indicating momentum conservation. The peak amplitude

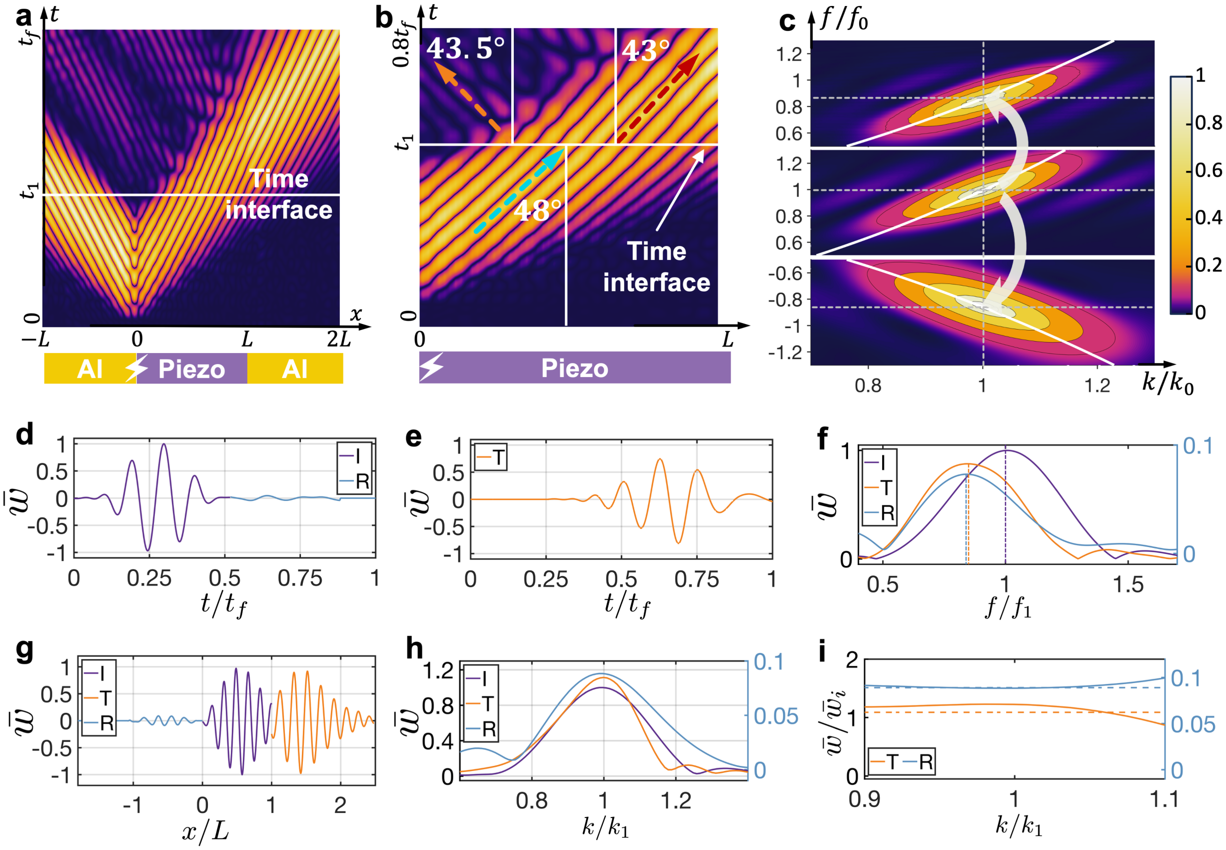

FIG. S8. **Temporal refraction and reflection in the metabeam with switch from OFF to ON. a** (**b**) The top panels show the simulation (**a**) and experiment (**b**) of wave scattering from an incident wave packet consisting of 3 cycles in the time domain, with $t_f = 1.1\,\text{ms}$ and $t_1 = 0.44\,\text{ms}$, at a time interface in a spacetime diagram. The bottom panels depict the system, with $L = 0.32\,\text{m}$, composed of two aluminum beams (Al) and a piezo-metabeam (Piezo), with the excitation (lightning symbol) located at the left interface. **c** The 2D Fourier transform of the experimental data shown in **b**. **d** The incident (purple) and reflected (blue) signals measured at $x = 0.05L$. **e** The refracted signal (orange) observed at $x = L$. **f** The spectral analysis of the time-domain signals from **d** and **e**. **g** The incident spatial profile (purple) measured at $t = 1/3t_f$, along with the reflected and transmitted spatial profiles (blue and orange, respectively) at $t = 2/3t_f$. **h** The spectral analysis of the spatial-domain signals from **g**. **i** The normalized spectral data for the reflected and refracted waves in **h**, each normalized by the amplitude distribution of the incident wave.

shifts from 1 in the incident wave to 1.5 in the refracted wave and 0.5 in the reflected wave, aligning with the results calculated using the Fresnel equations in Eq. (9) of the main text.

Furthermore, Fig. S7h presents the normalized amplitude distributions of the incident, transmitted, and reflected waves, with each normalized by the amplitude of the incident wave. This confirms that the amplitude ratio is independent of the wavenumber (frequency), as predicted by Eq. (7) of the main text. Additionally, the phase factors are deduced from the wave packet dynamics shown in Fig. S7i. The phase of the transmitted wave remains unchanged relative to the incident wave, while the phase of the reflected wave shifts by π relative to the incident wave across different wavenumbers, consistent with Eq. (9) of the main text.

5. REFRACTION AND REFLECTION AT A TIME INTERFACE FOR THE SWITCH FROM OFF TO ON IN EXPERIMENT

In this section, we examine temporal refraction and reflection during a switch transition from OFF to ON for an incident wave with a frequency of 6 kHz. The setup and parameters are identical to those in Fig. 2 of the main text. In this scenario, the refractive index ratio is $n_1/n_0 = 1.17$, and the impedance ratio is $Z_1/Z_0 = 0.85$. In Fig. S8a, the incident wave splits into a refracted wave and a reflected wave after passing through the time interface. In Fig. S8b, the incident angle of the plane waves is $\alpha_i = 48°$, with refracted and reflected angles of $\alpha_t = 43°$ and $\alpha_r = 43.5°$, respectively. The ratio $\tan\alpha_t/\tan\alpha_i = 0.84$ closely matches the refractive index ratio $n_1/n_2 = 0.85$, validating Snell's law as described in Eq. (S12) of the main text.

A 2D Fourier transform is applied to the data in Fig. S8a, with the results shown in Fig. S8c. In Fig. S8b, the frequency of the incident wave shifts from f_0 to $0.83f_0$ and $-0.83f_0$, while the wavenumber remains constant. To further confirm the frequency conversion and wavenumber invariance, time-domain signals measured at $x/L = 0.05$ and $x/L = 1$

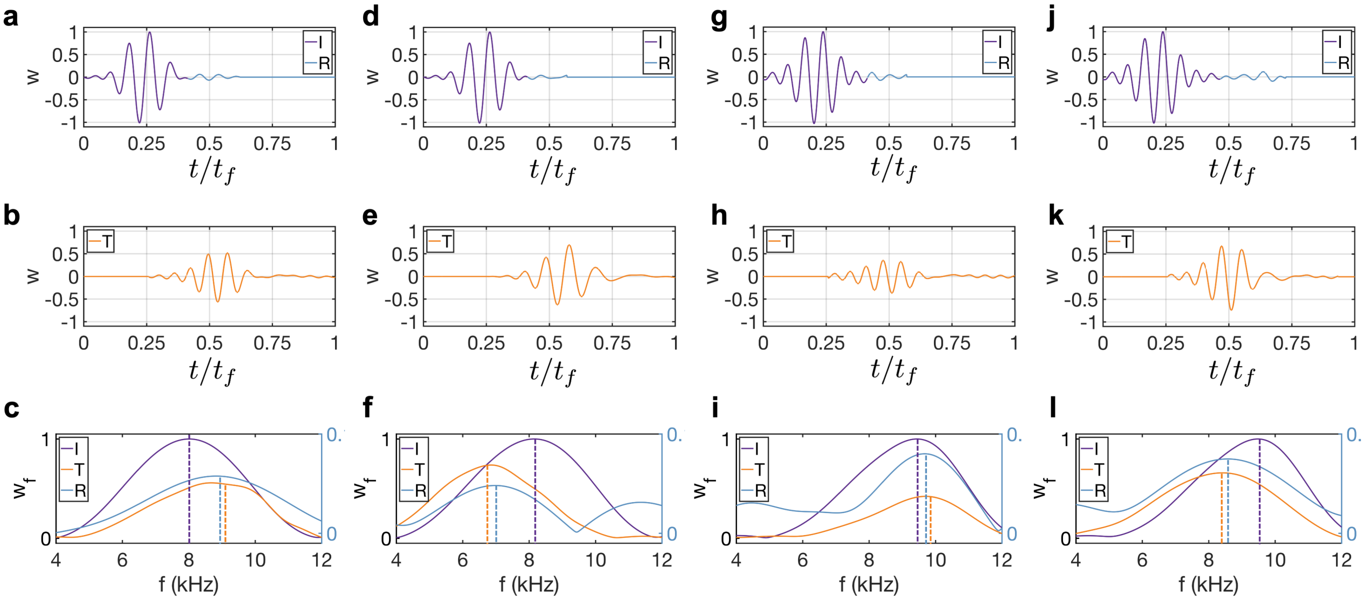

FIG. S9. **Spectral analysis of wave refraction and reflection at a time interface across different frequencies. a** (**d**) The incident temporal profile (purple) with an excitation frequency of 8 kHz, measured at $t = 1/3t_f$, and the reflected temporal profile (orange) at $t = 2/3t_f$. The switch transitions from ON to OFF (**a**) and from OFF to ON (**d**). **b** (**e**) The reflected and refracted temporal profiles (blue) at $t = 2/3t_f$. **c** (**f**) The spectral analysis of the incident, refracted, and reflected waves. **g** (**j**) The incident temporal profile (purple) with an excitation frequency of 10 kHz, measured at $t = 1/3t_f$, and the reflected temporal profile (orange) at $t = 2/3t_f$. The switch transitions from ON to OFF (**g**) and from OFF to ON (**j**). **h** (**k**) The reflected and refracted temporal profiles (blue) at $t = 2/3t_f$. **i** (**l**) The spectral analysis of the incident, refracted, and reflected waves.

are shown in Fig. S8d,e, where three distinct wave packets corresponding to the incident, refracted, and reflected waves are clearly visible. The normalized frequencies $f_t/f_0 = 0.83$ for the refracted wave and $f_r/f_0 = 0.83$ for the reflected wave quantitatively confirm the frequency shift relative to the incident wave, as shown in Fig. S8f, indicating a breakdown of energy conservation. Additionally, the spatial-domain signals measured at $t/t_f = 1/3$ and $t/t_f = 2/3$ are shown in Fig. S8g. The central wavenumbers k_t for the refracted wave and k_r for the reflected wave are consistent with the central wavenumber k_1 of the incident wave, as depicted in Fig. S8h, demonstrating the conservation of momentum. The normalized spectral data for the refracted and reflected waves is presented in Fig. S8i, where the normalized amplitudes are independent of the wavenumber and closely align with the theoretical predictions, thereby verifying the Fresnel equation in Eq. (9) of the main text.

6. REFRACTION AND REFLECTION AT A TIME INTERFACE FOR DIFFERENT FREQUENCIES IN THE EXPERIMENT

In this section, we examine wave refraction and reflection at different excitation frequencies, specifically 8 kHz (Fig. S9a–f) and 10 kHz (Fig. S9g–l), for switching transitions from ON to OFF and from OFF to ON, respectively. The excitation frequency refers to the frequency of the signal generated by the function generator, which may differ slightly from the incident frequency, defined as the peak position in the wave spectrum. The switching time in these cases is the same as that used for the case with an excitation frequency of 6 kHz.

As shown in Fig. S9c (f), the frequencies of the refracted and reflected waves shift from 8 kHz (incident wave) to 9 kHz and 7 kHz, respectively. In Fig. S9i (l), the frequencies of the refracted and reflected waves shift from 9.5 kHz (incident wave) to 9.8 kHz and 8.5 kHz, respectively.

For the 10 kHz case, the frequency shift does not satisfy Snell's law precisely. This discrepancy arises because the relatively high frequency leads to a smaller wavelength, increasing the ratio of the unit cell length to the wavelength. Consequently, the long-wave approximation is less valid, and the metabeam can no longer be considered a homogeneous beam. Furthermore, at higher frequencies, the homogeneous Euler-Bernoulli beam model becomes invalid, making the reflection and refraction less distinguishable and leading to inaccuracies in the frequency shift.

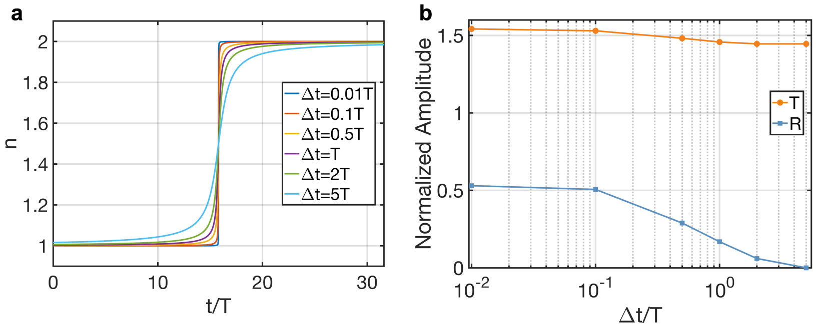

FIG. S10. **The effect of finite switching time.** **a** Different waveforms of $n(t)$ with parameters $\delta = 0.5$ and $\alpha = 1$. **b** Temporal refraction and reflection ratios as a function of $\Delta t/T$, where T is the period of the incident wave.

7. NUMERICAL INVESTIGATION OF THE EFFECT OF FINITE SWITCHING TIME

In the experiment, the switch does not transition instantaneously between states. In this section, we analyze the effect of finite switching time on the amplitudes of the refracted and reflected waves. To study this, various smooth time boundaries are modeled using the analytical function $n(t) = \frac{\Delta n}{\pi}\arctan\left(\frac{t-t_c}{\Delta t}\right) + n_0 + \frac{\Delta n}{2}$, where n_0 and $\Delta n = n_0$ represent the initial and changed refractive indices, and $\Delta t/T$ determines the sharpness of the waveform. Here, T is the period of the incident wave.

In Fig. S10a, the smooth step function is displayed for different values of $\Delta t/T$. The corresponding normalized amplitudes of the refracted and reflected waves, relative to the incident wave, are shown in Fig. S10b. The numerical setup in this section is the same as that described in Part B of Supplementary Section IV. When $\Delta t/T$ is very small (less than 0.1), the amplitudes of both the refracted and reflected waves remain constant and closely align with the theoretical predictions from Fresnel's formula. As long as $\Delta t/T$ stays within this range, the time interface can be regarded as ideal. In our experiment, $\Delta t/T = 0.001$, which is much smaller than 0.1, confirming that the interface behaves as an ideal time interface.

If $\Delta t/T$ exceeds 0.1, the amplitudes of both the refracted and reflected waves decrease as $\Delta t/T$ increases. However, the amplitude of the refracted wave approaches a finite value of $\sqrt{2}$, while the amplitude of the reflected wave diminishes to zero. This indicates that no reflected wave is generated when the refractive index changes very gradually. This behavior can be explained by the adiabatic theorem, which states that a system will remain in the same eigenstate if its parameters vary slowly enough. In the adiabatic limit, the wave's evolution can be described by [**? ?**]:

$$w(x,t) = \frac{A_i}{\sqrt{\omega(t)}} e^{ikx - \int_{t_0}^{t} \omega(t')dt'}. \tag{S2}$$

In this scenario, the wave remains a right-propagating wave, with its amplitude and frequency gradually changing over time and no reflected wave being generated. Since the ratio of the final frequency to the initial frequency is $\sqrt{2}$, the normalized amplitude of the refracted wave becomes $\sqrt{2}$, consistent with the results shown in Fig. S10b. Between the sudden-change limit and the adiabatic limit, the normalized amplitudes vary continuously as $\Delta t/T$ increases, falling within the range defined by these two extremes.

8. NUMERICAL STUDY OF TEMPORAL REFRACTION AND REFLECTION OF AN ASYMMETRIC PULSE

In this section, we demonstrate that the observed reflection is a temporal reflection rather than a spatial one. To highlight this distinction, we consider the scattering of an asymmetric pulse at a temporal interface. The simulation setup is identical to that described in Supplementary Section 4B. As shown in Fig. S11a, the spacetime diagram captures the behavior of the pulse upon encountering the interface.

Key differences between spatial and temporal reflections are evident in the order of pulse peaks. For spatial reflection, the higher peak of the incident pulse appears first, followed by the lower peak. In contrast, temporal reflection reverses this order: the lower peak arrives first, and the higher peak follows. This reversal in the time domain is shown in the normalized signals in Fig. S11b. Here, the incident ($\bar{w}_i$) and reflected ($\bar{w}_r$) signals, measured at $x/L = 0.3$, clearly demonstrate this inversion. In the spatial domain, the incident waves are shown in Fig. S11c. Fig. S11d displays the refracted ($\bar{w}_t$) and reflected ($\bar{w}_r$) signals, which are normalized and measured at $t/t_f = 0.3$. The reflected wave packet with the smaller peak appears first, followed by the reflected wave packet with the larger peak, which is opposite to the order observed in spatial reflection.

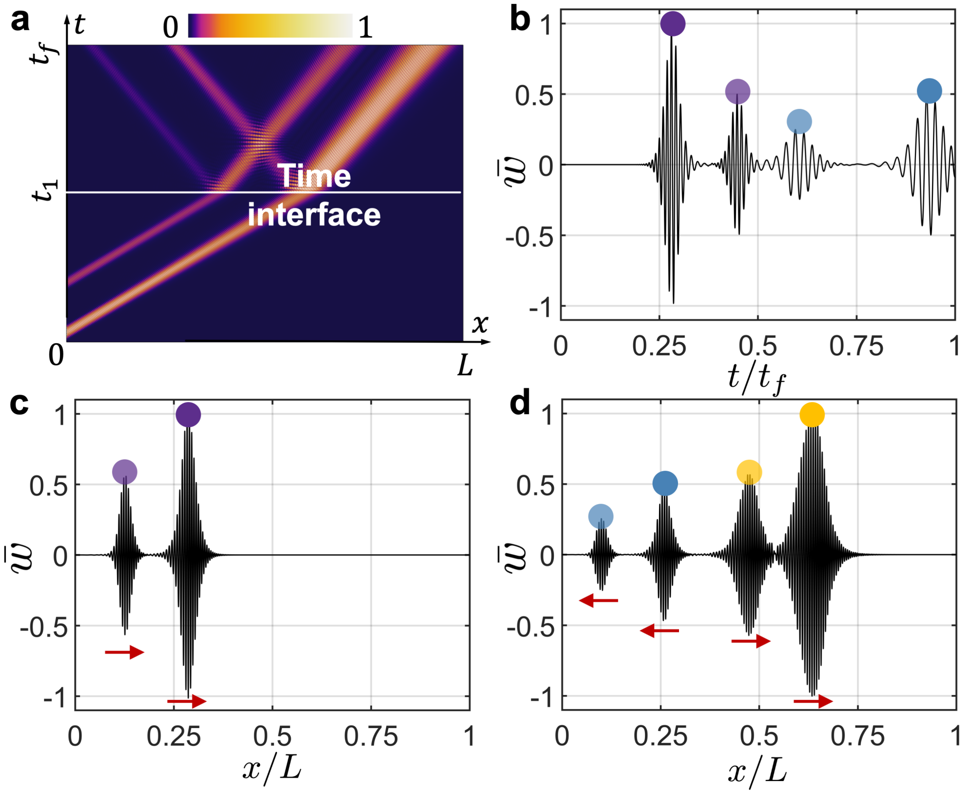

FIG. S11. **Refraction and reflection of an asymmetric pulse at a time interface.** **a** The spacetime diagram of a simulated asymmetric pulse scattering at a temporal interface. **b** The normalized incident ($\bar{w}_i$) and reflected ($\bar{w}_r$) signals measured at $x/L = 0.3$. The purple wave packet represents the incident wave with a higher amplitude, while the light purple wave packet corresponds to the incident wave with a lower amplitude. Similarly, the blue wave packet represents the reflected wave generated by the higher-amplitude incident wave, and the light blue wave packet corresponds to the reflected wave generated by the lower-amplitude incident wave. **c** The normalized incident ($\bar{w}_i$) signal measured at $t/t_f = 0.3$. The purple wave packet represents the incident wave with a higher amplitude, while the light purple wave packet corresponds to the incident wave with a lower amplitude. **d** The normalized refracted ($\bar{w}_t$) and reflected ($\bar{w}_r$) signals measured at $t/t_f = 0.3$. The orange wave packet represents the refracted wave with a higher amplitude, while the light orange wave packet corresponds to the incident wave with a lower amplitude. Similarly, the blue wave packet represents the reflected wave generated by the higher-amplitude incident wave, and the light blue wave packet corresponds to the reflected wave generated by the lower-amplitude incident wave.

9. DERIVATION OF TEMPORAL CONTINUITY CONDITIONS

The equation of motion for the Euler-Bernoulli beam is given by:

$$\partial_t p = \partial_{xx} M + q(t), \tag{S3}$$

where $p = \rho A \partial_t w$ represents the momentum, M is the bending moment, and q is a time dependent external force. Meanwhile, the bending curvature κ is defined as

$$\kappa = \partial_{xx} w. \tag{S4}$$

The bending momentum and bending curvature satisfy the constitutive relation

$$M = -D(t)\kappa. \tag{S5}$$

where $D(t) = E(t)I$ is the time-dependent bending stiffness, $E(t)$ is the time-dependent Young's modulus, and I it the second moment of area. Substituting Eq. (S5) and Eq. (S4) into the equation of motion (Eq. (S3)) yields the governing equations for the Euler-Bernoulli beam, as presented in Eq. (1) of the main text

$$\frac{\partial}{\partial t}\left(\rho A \frac{\partial w(x,t)}{\partial t}\right) + \frac{\partial^2}{\partial x^2}\left(D(t)\frac{\partial^2 w(x,t)}{\partial x^2}\right) = q(t). \tag{S6}$$

Integrating Eq. (S6) from initial time t' to an arbitrary time t gives

$$\rho A \frac{\partial w(x,t)}{\partial t}\bigg|_{t'}^{t} + \int_{t'}^{t} dt D(t)\frac{\partial^4 w(x,t)}{\partial x^4} = \int_{t'}^{t} q(t)dt. \tag{S7}$$

Taking $t' = t_1^- = t_1 - \epsilon$ to $t = t_1^+ = t_1 + \epsilon$ with a $\epsilon \to 0^+$, we expect that the second term in Eq. (S7) is zero, due to the finite values of fields. The term on the right-hand side represents the impulse, which is not considered in our study and is therefore set to zero. Then, we obtain the first temporal boundary condition that describes the continuity of momentum:

$$\rho A \frac{\partial w}{\partial t}\Big|_{t=t_1^+} = \rho A \frac{\partial w}{\partial t}\Big|_{t=t_1^-}. \tag{S8}$$

Since the density is time-independent, Eq. (S8) implies the continuity of velocity

$$\frac{\partial w}{\partial t}\Big|_{t=t_1^+} = \frac{\partial w}{\partial t}\Big|_{t=t_1^-}. \tag{S9}$$

Similarly, integrating Eq. (S7) from t_1^- to t_1^+ as $\epsilon \to 0^+$ with respect to t without the impulse gives the second temporal boundary condition that describes the continuity of displacement:

$$w|_{t=t_1^+} = w|_{t=t_1^-}. \tag{S10}$$

10. RELATIONSHIP BETWEEN THE ANGLES OF INCIDENCE AND REFRACTION

In the main text, the Snell's law is written as

$$\omega_1 n_1 = \omega_0 n_0. \tag{S11}$$

The more familiar form describing the geometric relationship between the angles of the incident and refracted waves in a space-time diagram is presented as follows.

In the (x, ct) space, where c is a reference speed to maintain dimensional consistency, the angle α between the propagation direction of a plane wave (with phase velocity ω/k) and the time axis satisfies the relation $\tan\alpha = \omega/(kc) = k/(nc)$. This results in the geometric relationship between the angle of incidence and the angle of refraction:

$$\frac{\tan\alpha_0}{\tan\alpha_1} = \frac{n_1}{n_0}. \tag{S12}$$

Eq. (S12) can be interpreted as the temporal Snell's law, describing the geometric relationship between the angles of the incident and refracted waves in a space-time diagram. This is analogous to the traditional Snell's law, which applies to wave propagation in two-dimensional space.

The dispersion relation of flexural waves is a quadratic function, making them dispersive, meaning the propagation direction of a wave packet differs from that of a plane wave. We now explore the geometric relationship between the incident and refracted angles of the wave packet. The angle between the propagation direction of the wave packet and the time axis is defined as $\tan\beta = v_g/c$, where the group velocity $v_g = d\omega/dk = 2k\sqrt{D/\rho A} = 2k/n$. Therefore, the geometric relationship between the incident and refracted angles of the wave packet is

$$\frac{\tan\beta_0}{\tan\beta_1} = \frac{n_1}{n_0}. \tag{S13}$$

Interestingly, this relationship is the same as the temporal Snell's law for plane waves.

Fig. S12 shows the relationship between the angles of incidence and refraction in a space-time diagram. Here, the angle of the incident plane wave α_i, the angle of the refracted plane wave α_t, and the angle of the reflected plane wave α_r are $49°, 52°$, and $52.5°$, respectively. The ratios $\tan\alpha_i/\tan\alpha_t = 0.9$ and $\tan\alpha_i/\tan\alpha_r = 0.88$ are close to the refractive index ratio $n_1/n_0 = 0.85$, confirming the temporal Snell's law in Eq. (S12). The geometric relation of the wave packet in Eq. (S13) is verified in a longer metabeam using 5-cycle tone-burst excitation, as detailed in Supplementary Section 4B.

11. JUSTIFICATION OF THE EULER–BERNOULLI MODEL: TIMOSHENKO EFFECTS, MODE TRUNCATION, DAMPING, AND NONLINEARITY

For a Timoshenko beam, the coupled equations for the transverse displacement $w(x, t)$ and the cross-sectional rotation $\phi(x, t)$ are given by:

$$\begin{aligned} \rho A \frac{\partial^2 w}{\partial t^2} &= \frac{\partial}{\partial x}\left[\kappa AG\left(\frac{\partial w}{\partial x} - \phi\right)\right], \\ \rho I \frac{\partial^2 \phi}{\partial t^2} &= \frac{\partial}{\partial x}\left(EI\frac{\partial \phi}{\partial x}\right) + \kappa AG\left(\frac{\partial w}{\partial x} - \phi\right), \end{aligned} \tag{S14}$$

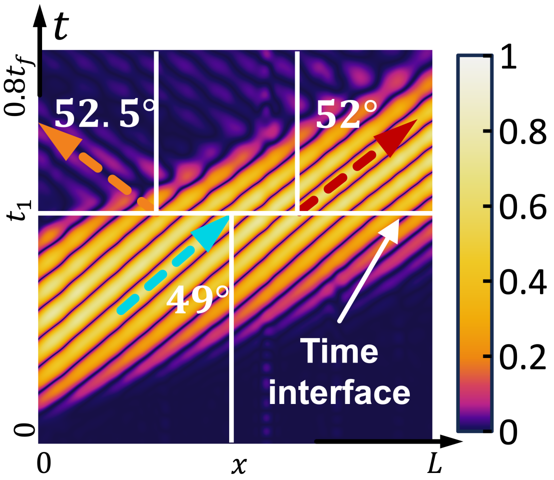

FIG. S12. **Relationship between the angles of incidence, refraction, and reflection**.

where ρ is the material density, A is the cross-sectional area, I is the area moment of inertia, E is Young's modulus, G is the shear modulus, and $\kappa = 5/6$ is the shear correction factor.

Assuming harmonic wave solutions of the form:

$$w(x,t) = We^{i(kx-\omega t)}, \quad \phi(x,t) = \Phi e^{i(kx-\omega t)}, \tag{S15}$$

the equations reduce to a compact matrix form:

$$\begin{pmatrix} \kappa AGk^2 - \omega^2 \rho A & i\kappa AGk \\ -i\kappa AGk & EIk^2 + \kappa AG - \omega^2 \rho I \end{pmatrix} \begin{pmatrix} W \\ \Phi \end{pmatrix} = \mathbf{0}. \tag{S16}$$

Setting the determinant of the coefficient matrix to zero yields the dispersion relation:

$$\frac{\rho^2 AI}{\kappa AG}\omega^4 - \left[\rho A + \left(\rho I + \frac{EI\rho A}{\kappa AG}\right)k^2\right]\omega^2 + EIk^4 = 0. \tag{S17}$$

Solving for ω as a function of k, we obtain the positive real branch:

$$\omega = \sqrt{\frac{\rho A + \left(\rho I + \frac{EI\rho A}{\kappa AG}\right)k^2 + \sqrt{\left[\rho A + \left(\rho I + \frac{EI\rho A}{\kappa AG}\right)k^2\right]^2 - 4\frac{\rho^2 AI}{\kappa AG}EIk^4}}{2\frac{\rho^2 AI}{\kappa AG}}}. \tag{S18}$$

The corresponding normalized eigenvector is given by:

$$\psi(\omega,k) = \frac{1}{\sqrt{\left(\kappa AGk^2 - \omega^2\right)^2 - \left(\kappa AGk\right)^2}} \begin{pmatrix} -i\kappa AGk \\ \kappa AGk^2 - \omega^2 \end{pmatrix}, \tag{S19}$$

and the complete time-harmonic solution becomes:

$$\Psi(x,t) = \psi(\omega,k)\, e^{i(kx-\omega t)}. \tag{S20}$$

Suppose that at a specific time $t = t_0$, the beam's effective stiffness changes abruptly due to the switching of an external electronic circuit. In our case, this change primarily affects the bending stiffness. We define the effective bending stiffness before and after the temporal interface as:

$$E_0 I \quad \text{and} \quad E_1 I, \tag{S21}$$

respectively. The piezoelectric patches do not affect the shear term or the mass parameters. Therefore, we assume that the shear term κAG and the mass parameters ρA and ρI remain unchanged.

Under this condition, Snell's law for the temporal interface can be expressed as:

$$\omega_0 n_0 = \omega_1 n_1, \tag{S22}$$

where n_0 and n_1 are the effective refractive indices corresponding to stiffnesses E_0I and E_1I, respectively, and are computed via Eq. (S18).

We assume the wavefield before the temporal interface takes the form:

$$\Psi_0(x,t) = \psi_0(\omega_0,k)\, e^{ikx-i\omega_0 t}, \tag{S23}$$

where $\psi_0(\omega_0,k)$ is the eigenvector in Eq. (S19) for frequency ω_0. While the wavefield after the interface contains both forward- and backward-propagating components:

$$\Psi_1(x,t) = T\,\psi_1(\omega_1,k)\, e^{ikx-i\omega_1 t} + R\,\psi_1(\omega_1,k)\, e^{ikx+i\omega_1 t}. \tag{S24}$$

where $\psi_1(\omega_1,k)$ is the eigenvector in Eq. (S19) for frequency ω_1, T is the refracted coefficient, and R is the reflected coefficient. At the temporal interface $t=t_0$, the continuity conditions for displacement and velocity are:

$$\Psi_0 = \Psi_1, \quad \partial_t\Psi_0 = \partial_t\Psi_1. \tag{S25}$$

Substituting the waveforms into these conditions and evaluating at $t=t_0$, we obtain:

$$\begin{aligned}\psi_0(\omega_0,k) &= T\,\psi_1(\omega_1,k) + R\,\psi_1(\omega_1,k),\\ \omega_0\,\psi_0(\omega_0,k) &= \omega_1 T\,\psi_1(\omega_1,k) - \omega_1 R\,\psi_1(\omega_1,k).\end{aligned} \tag{S26}$$

We now take the inner product of both equations with the dual (left) eigenvector $\psi_1^\dagger(\omega_1,k)$. This yields:

$$\begin{aligned}\psi_1^\dagger(\omega_1,k)\psi_0(\omega_0,k) &= T+R,\\ \omega_0\psi_1^\dagger(\omega_1,k)\psi_0(\omega_0,k) &= \omega_1(T-R).\end{aligned} \tag{S27}$$

Solving this system of equations, we obtain the Fresnel-type refraction and reflection coefficients:

$$\begin{aligned}T &= \frac{\omega_1+\omega_0}{2\omega_0}\,\psi_1^\dagger(\omega_1,k)\psi_0(\omega_0,k),\\ R &= \frac{\omega_1-\omega_0}{2\omega_0}\,\psi_1^\dagger(\omega_1,k)\psi_0(\omega_0,k).\end{aligned} \tag{S28}$$

These expressions generalize the Fresnel equations to the Timoshenko beam case, where the reflection and refraction amplitudes are determined by both frequency shift and mode overlap across the temporal interface.

We now turn to the numerical evaluation of Snell's law and Fresnel coefficients using the Timoshenko beam model, and compare the results with those obtained from the Euler–Bernoulli beam model and COMSOL simulation. As shown in Fig. S13, the dispersion curves from all three models closely match, confirming the validity of the Euler–Bernoulli approximation. When the bending stiffness changes from $D/D_0 = 1$ to $D/D_0 = 0.85^2$, the normalized frequencies for the Timoshenko beam, Euler–Bernoulli beam, and COMSOL simulation change from $0.991, 0.989, 1$ to $0.844, 0.842, 0.85$, respectively. This yields corresponding ratios ω_1/ω_0 of 0.8517, 0.8514, and 0.850, respectively.

Moreover, the mode overlap term $\psi_1^\dagger(\omega,k)\psi_0(\omega,k)$, which appears in the Fresnel equations (Eq. S28), evaluates to 0.999999311089990, indicating that the mode shapes before and after switching remain nearly identical. Therefore, the reflection and refraction coefficients predicted by the Timoshenko and Euler–Bernoulli models are virtually indistinguishable. The differences are negligible in practical terms.

This agreement can be understood by introducing the characteristic shear length scale

$$\ell = \sqrt{\frac{EI}{\kappa GA}}, \tag{S29}$$

which leads to the dimensionless dynamic slenderness parameter $\Lambda = \ell k$. In our setup, $\Lambda \sim 10^{-4}$, indicating that shear effects are minimal and the Euler–Bernoulli model is valid.

To further validate this conclusion, we consider a more extreme case where the stiffness drops from $D/D_0 = 1$ to $D/D_0 = 0.25$ at the temporal interface. The normalized frequencies change from $0.991, 0.989, 1$ to $0.498, 0.497, 0.5$ for the Timoshenko beam, Euler–Bernoulli beam, and COMSOL, respectively, yielding $\omega_1/\omega_0 = 0.5025$, 0.5025, and 0.500. The mode overlap in this case is still very high: $\psi_1^\dagger(\omega,k)\psi_0(\omega,k) = 0.999998443354908$. Again, the Fresnel coefficients predicted by both beam models are nearly identical.

These results confirm that even under strong modulation, the Euler–Bernoulli beam theory provides sufficiently accurate predictions, and the effects of shear deformation and rotary inertia are negligible for our study. The small discrepancies observed are likely attributed to two factors: (i) incomplete termination of low-frequency incident signals before reaching the temporal boundary, and (ii) possible breakdown of the homogeneous beam assumption at high frequencies due to microstructural effects. These factors, rather than the beam model itself, account for the minor deviations between theory and experiment.

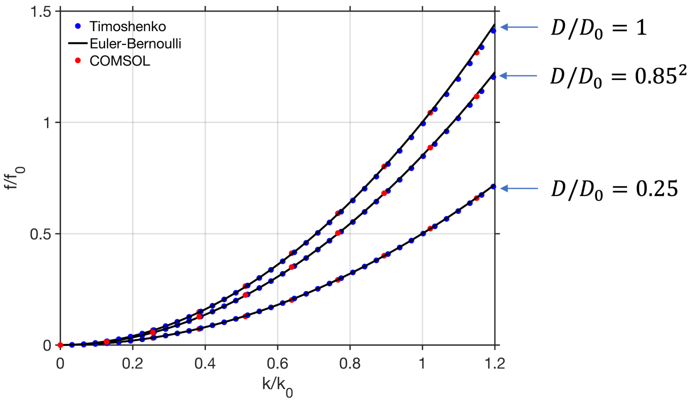

FIG. S13. Dispersion curves obtained from the Timoshenko beam model, the Euler–Bernoulli model, and COMSOL simulation. The top branch corresponds to the case with the circuit switch turned off. The bottom branches correspond to circuits with $R_1 = 5\,\mathrm{k\Omega}$ ($D/D_0 = 0.85^2$, used in the experiment) and $R_1 = 5.6\,\mathrm{k\Omega}$ ($D/D_0 = 0.25$, used in Fig. S7(a)).

We now turn to discuss the negligibility of other modes. In our study, the excitation frequency for temporal refraction and reflection is 6–10 kHz, which is significantly lower than the characteristic frequencies of shear modes ($\sim$776 kHz) and higher-order bending modes (above 80 kHz). The dispersion relations and mode shapes confirm that these modes lie far outside the excitation range. Moreover, the amplitude of the incident tone-burst signal drops below 0.01 at frequencies above 30 kHz, effectively suppressing the excitation of higher-order modes in practice. In experiments, a 1–40 kHz bandpass filter is also applied to further suppress potential high-frequency or non-flexural contributions.

Regarding longitudinal waves, they can in principle be excited by the piezoelectric actuator. However, the group velocity of the longitudinal mode is nearly eight times that of the fundamental flexural mode, meaning that any longitudinal wave passes through the time-varying segment well before the temporal modulation is active. Moreover, both the experimental and numerical signals focus on the transverse displacement $w(x,t)$; longitudinal displacement is neither measured in experiments nor extracted in simulations. Therefore, longitudinal waves do not affect the observed wavefields in either experiment or simulation. In experiments, a 1–40 kHz bandpass filter is also applied to further suppress potential high-frequency or non-flexural contributions.

Note on Damping Effects: In our system, damping arises from two sources: the elastic beam and the electrical circuits. For the beam, the intrinsic damping is characterized by a low material loss factor ($\eta \sim 10^{-4}$), resulting in negligible attenuation ($< 0.1\%$ amplitude loss over the beam length). For the circuit, effective damping depends on the resistor value R_0, which can introduce either loss or gain. By tuning $R_0 = 1$ MΩ, we balance these effects to minimize amplitude variation. As damping has minimal impact within the experimental timescales, it is omitted from the main theoretical model.

Note on Nonlinearity: In our study, both structural and circuit-level nonlinearities are negligible under the operating conditions. The maximum beam deflection is less than 0.001 mm—well below the geometric nonlinearity threshold ($w/h < 0.1$), and material strains remain within the elastic regime. Piezoelectric patches operate below ±40 V, avoiding nonlinear dielectric behavior. On the circuit side, capacitors and resistors exhibit minimal voltage dependence, and operational amplifiers function well within their linear range. No harmonic distortion or waveform asymmetry is observed experimentally, and all FFT spectra agree with linear theory. Thus, the system behavior is accurately captured by a linear model, and the effect of nonlinearity can be safely ignored for the amplitude range used in this work.

12. NOETHER'S THEOREM AND CONSERVATION LAWS

A. Complex scalar field theory for the Euler-Bernoulli beam

As we know, when a flexural incident wave encounters an interface where the refractive index of the beam changes abruptly, it splits into a refracted wave and a reflected wave, as shown in Fig. S14a,b. Remarkably, the governing equation of the Euler-Bernoulli beam model inherently supports space-time duality, implying temporal analogs of reflection and refraction when a flexural wave encounters a time boundary, as illustrated in Fig. S14c,d. Wave scattering at both spatial and temporal boundaries adheres to Noether's theorem, which reveals the fundamental connection between the symmetries of a physical system and its conservation laws. In systems with abrupt spatial changes, the breakdown of space translation invariance leads to the non-conservation of momentum. However, the system remains invariant in the time direction, preserving time translation invariance and, consequently, the conservation of energy. In this section, energy and momentum are derived as Noether's charges in accordance with Noether's theorem.

In this paper, we examine wave propagation in the frequency domain, which involves complex analysis. There are two methods for deriving Noether's charge. The first method involves obtaining the expression for Noether's charge using real

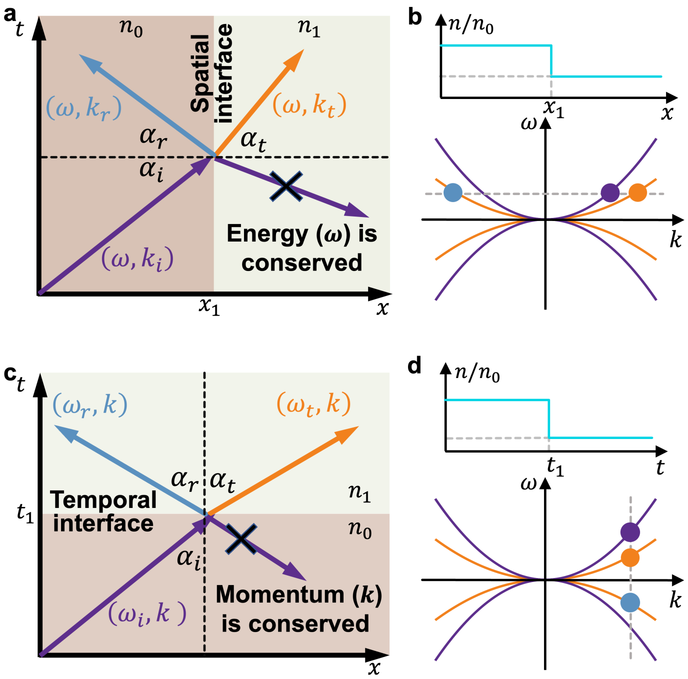

FIG. S14. **Refraction and reflection of flexural waves at a time interface.a** (**c**) Spacetime diagram of wave refraction and reflection at a spatial (temporal) interface. The subscripts i, r, and t correspond to the incident, reflected, and refracted waves, respectively. **b** (**d**) The top panel shows the index of refraction versus $x\,(t)$, with an abrupt change at $x_1\,(t_1)$. The bottom panel displays the dispersion curves: the medium before (after) $x_1\,(t_1)$ is represented by a purple (orange) solid line. The blue, red, and yellow points correspond to the incident, reflected, and refracted waves, respectively.

scalar field theory, followed by applying a periodic average to derive the corresponding charge in the complex domain [? ?]. The second method derives the expression for Noether's charge directly from complex scalar field theory, avoiding time averaging. In this study, we employ the second method.

The complex scalar field is defined as $w(x,t) = \left[w_r(x,t) + i w_i(x,t)\right]/\sqrt{2}$, constructed from two identical real fields, $w_r(x,t)$ and $w_i(x,t)$ [? ? ?]. For convenience, we use $w(x,t)$ and $w^\dagger(x,t)$ as independent variables instead of $w_r(x,t)$ and $w_i(x,t)$. The Lagrangian for the Euler-Bernoulli beam can be extended from that of real scalar field theory [?] as follows:

$$\mathcal{L} = \frac{1}{2}\rho A \partial_t w^\dagger(x,t)\partial_t w(x,t) - \frac{1}{2} EI \partial_{xx} w^\dagger(x,t)\partial_{xx} w(x,t) \tag{S30}$$

And the action S, the time integral of the Lagrangian $\mathcal{L}$, can be written as

$$S = \int \mathcal{L} dt = \int \mathcal{L}\left(w_t, w_t^\dagger, w_{xx}, w_{xx}^\dagger\right) dx dt \tag{S31}$$

The principle of least action states [?]

$$\begin{aligned}
0 &= \delta S \\
&= \int dxdt \Bigg\{ \frac{\partial \mathcal{L}}{\partial\left(\partial_t w\right)} \delta\left(\partial_t w\right) + \frac{\partial \mathcal{L}}{\partial\left(\partial_{xx} w\right)} \delta\left(\partial_{xx} w\right) + \frac{\partial \mathcal{L}}{\partial\left(\partial_t w^\dagger\right)} \delta\left(\partial_t w^\dagger\right) + \frac{\partial \mathcal{L}}{\partial\left(\partial_{xx} w^\dagger\right)} \delta\left(\partial_{xx} w^\dagger\right) \Bigg\} \\
&= \int dxdt \Bigg\{ \partial_t\left(\frac{\partial \mathcal{L}}{\partial\left(\partial_t w\right)}\delta w\right) - \partial_t\left(\frac{\partial \mathcal{L}}{\partial\left(\partial_t w\right)}\right)\delta w + \partial_x\left(\frac{\partial \mathcal{L}}{\partial\left(\partial_{xx} w\right)}\partial_x \delta w\right) - \partial_x\left(\partial_x \frac{\partial \mathcal{L}}{\partial\left(\partial_{xx} w\right)}\delta w\right) + \partial_{xx}\left(\frac{\partial \mathcal{L}}{\partial\left(\partial_{xx} w\right)}\right)\delta w \\
&\quad + \partial_t\left(\frac{\partial \mathcal{L}}{\partial\left(\partial_t w^\dagger\right)}\delta w^\dagger\right) - \partial_t\left(\frac{\partial \mathcal{L}}{\partial\left(\partial_t w^\dagger\right)}\right)\delta w^\dagger + \partial_x\left(\frac{\partial \mathcal{L}}{\partial\left(\partial_{xx} w^\dagger\right)}\partial_x \delta w^\dagger\right) - \partial_x\left(\partial_x \frac{\partial \mathcal{L}}{\partial\left(\partial_{xx} w^\dagger\right)}\delta w^\dagger\right) + \partial_{xx}\left(\frac{\partial \mathcal{L}}{\partial\left(\partial_{xx} w^\dagger\right)}\right)\delta w^\dagger \Bigg\} \\
&= \int dxdt \Bigg\{ -\partial_t\left(\frac{\partial \mathcal{L}}{\partial\left(\partial_t w\right)}\right)\delta w + \partial_{xx}\left(\frac{\partial \mathcal{L}}{\partial\left(\partial_{xx} w\right)}\right)\delta w - \partial_t\left(\frac{\partial \mathcal{L}}{\partial\left(\partial_t w^\dagger\right)}\right)\delta w^\dagger + \partial_{xx}\left(\frac{\partial \mathcal{L}}{\partial\left(\partial_{xx} w^\dagger\right)}\right)\delta w^\dagger \Bigg\}
\end{aligned} \tag{S32}$$

where the rules of variational operations can be found in [?]. By factoring out δw ($\delta w^\dagger$) from the first two terms (last two terms), we note that, since the integral must vanish for arbitrary δw ($\delta w^\dagger$), the quantity multiplying δw ($\delta w^\dagger$) must also vanish at all points. This leads us to the Euler-Lagrange equation of motion for the complex field:

$$\partial_t \left(\frac{\partial \mathcal{L}}{\partial \left(\partial_t w \right)} \right) - \partial_{xx} \left(\frac{\partial \mathcal{L}}{\partial \left(\partial_{xx} w \right)} \right) = 0 \tag{S33}$$

$$\partial_t \left(\frac{\partial \mathcal{L}}{\partial \left(\partial_t w^\dagger \right)} \right) - \partial_{xx} \left(\frac{\partial \mathcal{L}}{\partial \left(\partial_{xx} w^\dagger \right)} \right) = 0. \tag{S34}$$

B. Time translation symmetry and energy conservation

We can describe the infinitesimal translation of time as

$$t \rightarrow t + \delta t \tag{S35}$$

alternatively as a transformation of the field configuration

$$\begin{aligned} w(x,t) \rightarrow w(x,t) = w(x,t) + \delta t \partial_t w(x,t), \\ w^\dagger(x,t) \rightarrow w^\dagger(x,t) = w^\dagger(x,t) + \delta t \partial_t w^\dagger(x,t). \end{aligned} \tag{S36}$$

More generally, we can allow the action to change by a surface term, since the presence of such a term would not affect our derivation of the Euler-Lagrange equations of motion Eq. (S33,S34). The Lagrangian, therefore, must be invariant under Eq. (S35) up to a divergence:

$$\mathcal{L} \rightarrow \mathcal{L} + \delta t \partial_t \mathcal{L}. \tag{S37}$$

On the other hand, the change in the Lagrangian density $\mathcal{L}$ is then given by

$$\begin{aligned} \delta \mathcal{L} &= \frac{\partial \mathcal{L}}{\partial \left(\partial_t w \right)} \delta \left(\partial_t w \right) + \frac{\partial \mathcal{L}}{\partial \left(\partial_t w^\dagger \right)} \delta \left(\partial_t w^\dagger \right) + \frac{\partial \mathcal{L}}{\partial \left(\partial_{xx} w \right)} \delta \left(\partial_{xx} w \right) + \frac{\partial \mathcal{L}}{\partial \left(\partial_{xx} w^\dagger \right)} \delta \left(\partial_{xx} w^\dagger \right) \\ &= \frac{\partial \mathcal{L}}{\partial \left(\partial_t w \right)} \partial_t \left(\delta w \right) + \frac{\partial \mathcal{L}}{\partial \left(\partial_t w^\dagger \right)} \partial_t \left(\delta w^\dagger \right) + \frac{\partial \mathcal{L}}{\partial \left(\partial_{xx} w \right)} \partial_{xx} \left(\delta w \right) + \frac{\partial \mathcal{L}}{\partial \left(\partial_{xx} w^\dagger \right)} \partial_{xx} \left(\delta w^\dagger \right) \\ &= \delta t \left[\frac{\partial \mathcal{L}}{\partial \left(\partial_t w \right)} \partial_t \left(w_t \right) + \frac{\partial \mathcal{L}}{\partial \left(\partial_t w^\dagger \right)} \partial_t \left(w_t^\dagger \right) + \frac{\partial \mathcal{L}}{\partial \left(\partial_{xx} w \right)} \partial_{xx} \left(w_t \right) + \frac{\partial \mathcal{L}}{\partial \left(\partial_{xx} w^\dagger \right)} \partial_{xx} \left(w_t^\dagger \right) \right] \end{aligned} \tag{S38}$$

Multiplying Eq. (S33) with $\delta t w_t$ and Eq. (S34) with $\delta t w_t^\dagger$, and adding them into Eq. (S38) gives

$$\begin{aligned} \delta \mathcal{L} = \delta t \partial_t & \left(\frac{\partial \mathcal{L}}{\partial \left(\partial_t w \right)} w_t + \frac{\partial \mathcal{L}}{\partial \left(\partial_t w^\dagger \right)} w_t^\dagger \right) \\ & + \delta t \partial_x \left[\partial_x \left(\frac{\partial \mathcal{L}}{\partial \left(\partial_{xx} w \right)} \right) w_t + \partial_x \left(\frac{\partial \mathcal{L}}{\partial \left(\partial_{xx} w^\dagger \right)} \right) w_t^\dagger + \frac{\partial \mathcal{L}}{\partial \left(\partial_{xx} w \right)} w_{xt} + \frac{\partial \mathcal{L}}{\partial \left(\partial_{xx} w^\dagger \right)} w_{xt}^\dagger \right] \end{aligned} \tag{S39}$$

The Lagrangian density $\mathcal{L}$ could very well change by a divergence $\delta \mathcal{L} = \delta t \partial_t \mathcal{L}$. Therefore, the combination of Eq. (S39) and Eq. (S37) upon arbitrary infinitesimal time translation δt leads to

$$\partial_t j^{tt} + \partial_x j^{tx} = 0, \tag{S40}$$

where

$$\begin{aligned} j^{tt} &= \frac{\partial \mathcal{L}}{\partial \left(\partial_t w \right)} w_t + \frac{\partial \mathcal{L}}{\partial \left(\partial_t w^\dagger \right)} w_t^\dagger - \mathcal{L} \\ j^{tx} &= \partial_x \left(\frac{\partial \mathcal{L}}{\partial \left(\partial_{xx} w \right)} \right) w_t + \partial_x \left(\frac{\partial \mathcal{L}}{\partial \left(\partial_{xx} w^\dagger \right)} \right) w_t^\dagger + \frac{\partial \mathcal{L}}{\partial \left(\partial_{xx} w \right)} w_{xt} + \frac{\partial \mathcal{L}}{\partial \left(\partial_{xx} w^\dagger \right)} w_{xt}^\dagger \end{aligned} \tag{S41}$$

Then, performing the integration over x at constant time gives

$$\partial_t \int j^{tt} dx = 0, \tag{S42}$$

where $\int \partial_x j^{tx} dx = 0$ is used because this will vanish if the line is long enough [**?**]. Now we define $\mathcal{H}$ as the energy density:

$$\mathcal{H} = \frac{\partial \mathcal{L}}{\partial \left(\partial_t w \right)} \partial_t w + \frac{\partial \mathcal{L}}{\partial \left(\partial_t w^\dagger \right)} \partial_t w^\dagger - \mathcal{L} \tag{S43}$$

And the Hamiltonian (energy)

$$H = \int \mathcal{H} dx = \int dx \left(\frac{1}{2} \rho A \partial_t w^\dagger(x,t) \partial_t w(x,t) + \frac{1}{2} EI \partial_{xx} w^\dagger(x,t) \partial_{xx} w(x,t) \right). \tag{S44}$$

is conserved for system with time translation symmetry according to Eq. (S42). The energy before the switching event is

$$H_0 = \left(\frac{1}{2} \rho A \omega_0^2 + \frac{1}{2} E_0 I_0 k_0^4 \right) A_i^2 = \frac{1}{Z_0^2} \rho A A_i^2, \tag{S45}$$

whereas the energy density after the switching event is

$$H_1 = \left(\frac{1}{2} \rho A \omega_1^2 + \frac{1}{2} E_1 I_1 k_1^4 \right) \left(T^2 + R^2 \right) A_i^2 = \frac{Z_0^2 + Z_1^2}{2 Z_1^4} \rho A A_i^2 = \frac{Z_0^4 + Z_0^2 Z_1^2}{2 Z_1^4} H_0, \tag{S46}$$

where Eq. (9) in the main text is used. Now we can be easily verified that the energy in Eq. (S46) is not conserved:

$$H_1 \neq H_0 \tag{S47}$$

for temporal media with $Z_0 \neq Z_1$. We conclude that the breaking of time translation symmetry leads to the breakdown of the conservation of energy.

C. Space translation symmetry and momentum conservation

We can describe the infinitesimal translation of time as

$$x \to x + \delta x \tag{S48}$$

alternatively as a transformation of the field configuration

$$\begin{aligned} w(x,t) &\to w(x,t) = w(x,t) + \delta x \partial_x w(x,t), \\ w^\dagger(x,t) &\to w^\dagger(x,t) = w^\dagger(x,t) + \delta x \partial_x w^\dagger(x,t). \end{aligned} \tag{S49}$$

More generally, we can allow the action to change by a surface term, since the presence of such a term would not affect our derivation of the Euler-Lagrange equations of motion Eq. (S33,S34). The Lagrangian, therefore, must be invariant under Eq. (S48) up to a divergence:

$$\mathcal{L} \to \mathcal{L} + \delta x \partial_x \mathcal{L}. \tag{S50}$$

On the other hand, the change in the Lagrangian density $\mathcal{L}$ is then given by

$$\begin{aligned} \delta \mathcal{L} &= \frac{\partial \mathcal{L}}{\partial (\partial_t w)} \delta (\partial_t w) + \frac{\partial \mathcal{L}}{\partial (\partial_t w^\dagger)} \delta \left(\partial_t w^\dagger\right) + \frac{\partial \mathcal{L}}{\partial (\partial_{xx} w)} \delta (\partial_{xx} w) + \frac{\partial \mathcal{L}}{\partial (\partial_{xx} w^\dagger)} \delta \left(\partial_{xx} w^\dagger\right) \\ &= \delta x \left[\frac{\partial \mathcal{L}}{\partial (\partial_t w)} \partial_t (w_x) + \frac{\partial \mathcal{L}}{\partial (\partial_t w^\dagger)} \partial_t \left(w_x^\dagger\right) + \frac{\partial \mathcal{L}}{\partial (\partial_{xx} w)} \partial_{xx} (w_x) + \frac{\partial \mathcal{L}}{\partial (\partial_{xx} w^\dagger)} \partial_{xx} \left(w_x^\dagger\right) \right] \end{aligned} \tag{S51}$$

Multiplying Eq. (S33) with $\delta x w_x$ and Eq. (S34) with $\delta x w_x^\dagger$, and adding them into Eq. (S51) gives

$$\begin{aligned} \delta \mathcal{L} &= \delta x \partial_t \left(\frac{\partial \mathcal{L}}{\partial (\partial_t w)} w_x + \frac{\partial \mathcal{L}}{\partial (\partial_t w^\dagger)} w_x^\dagger \right) \\ &+ \delta x \partial_x \left[\partial_x \left(\frac{\partial \mathcal{L}}{\partial (\partial_{xx} w)} \right) w_x + \partial_x \left(\frac{\partial \mathcal{L}}{\partial (\partial_{xx} w^\dagger)} \right) w_x^\dagger + \frac{\partial \mathcal{L}}{\partial (\partial_{xx} w)} w_{xx} + \frac{\partial \mathcal{L}}{\partial (\partial_{xx} w^\dagger)} w_{xx}^\dagger \right] \end{aligned} \tag{S52}$$

The Lagrangian density $\mathcal{L}$ may change by a divergence, $\delta \mathcal{L} = \delta x \partial_x \mathcal{L}$. Therefore, combining Eq. (S51) and Eq. (S50) under an arbitrary infinitesimal time translation δx results in the following expression:

$$\partial_t j^{tx} + \partial_x j^{xx} = 0, \tag{S53}$$

where

$$\begin{aligned} j^{tx} &= \frac{\partial \mathcal{L}}{\partial (\partial_t w)} w_x + \frac{\partial \mathcal{L}}{\partial (\partial_t w^\dagger)} w_x^\dagger \\ j^{xx} &= \partial_x \left(\frac{\partial \mathcal{L}}{\partial (\partial_{xx} w)} \right) w_x + \partial_x \left(\frac{\partial \mathcal{L}}{\partial (\partial_{xx} w^\dagger)} \right) w_x^\dagger + \frac{\partial \mathcal{L}}{\partial (\partial_{xx} w)} w_{xx} + \frac{\partial \mathcal{L}}{\partial (\partial_{xx} w^\dagger)} w_{xx}^\dagger \end{aligned} \tag{S54}$$

Then, performing the integration over x at constant time gives

$$\partial_t \int j^{tx} dx = 0, \tag{S55}$$

where $\int \partial_x j^{xx} dx = 0$ is used because this will vanish if the line is long enough [**?**]. Now we define p as the momentum density:

$$p = j^{tx} = \frac{\partial \mathcal{L}}{\partial \left(\partial_t w\right)} \partial_x w + \frac{\partial \mathcal{L}}{\partial \left(\partial_t w^\dagger\right)} \partial_x w^\dagger \tag{S56}$$

The conserved charges (momentum) associated with spatial translations are

$$P = \int p dx = \int dx \rho A [\left(\partial_t w^\dagger\right) w_x + \left(\partial_t w\right) w_x^\dagger]. \tag{S57}$$

The momentum of the wave before the switching event is

$$P_0 = 2\rho A \omega_0 k_0 A_i^2, \tag{S58}$$

whereas the momentum of waves after the switching event is

$$P_1 = 2\rho A \omega_1 k_1 (T^2 - R^2) A_i^2. \tag{S59}$$

With the aid of Eq. (9) in the main text, the momentum conservation can be easily verified that

$$P_0 = P_1 = 2 Z_0 k_0^3 A_i^2. \tag{S60}$$

13. OPTIMIZATION METHOD FOR BROADBAND ANTI-REFLECTION AND WAVE AMPLIFICATION AT MULTIPLE TIME INTERFACES

In this section, we provide a detailed description of the optimization problem for designing temporal multilayer media aimed at eliminating broadband reflected waves and enhancing wave amplification.

For single-frequency reflected wave elimination, the optimization problem can be proposed as

$$\begin{array}{cl} \underset{n_1, t_2}{\text{minimize}} & |R(n_1, t_2, f_0 = 6 \text{ kHz})|^2 \\ \text{subject to} & n_0 \le n_1 \le 2n_0, \\ & \quad \Delta t_1 > 0 \end{array} \tag{S61}$$

For broadband reflected wave elimination, the optimization problem can be proposed as

$$\begin{array}{cl} \underset{\boldsymbol{n}, \boldsymbol{t}}{\text{minimize}} & \int_{f_a}^{f_b} |R(\boldsymbol{n}, \boldsymbol{t}), f_0|^2 df_0 \\ \text{subject to} & \min(n_0, n_{M+1}) \le n_i \le \max(n_0, n_{M+1}), \quad i = 1, \ldots, M \\ & \Delta t_j > 0, \quad j = 1, \ldots, M \end{array} \tag{S62}$$

where $f_a = 0.5 f_0$, $f_b = 1.5 f_0$, $M = 4$, $n_{M+1} = 2n_0$.

For wave amplification, the optimization problem can be proposed as

$$\begin{array}{cl} \underset{\boldsymbol{n}, \boldsymbol{t}}{\text{minimize}} & -|T(\boldsymbol{n}, \boldsymbol{t}, f_0 = 6 \text{ kHz})|^2 \\ \text{subject to} & 0 \le n_i \le 3n_0, \quad i = 1, \ldots, M \\ & \Delta t_j > 0, \quad j = 1, \ldots, M \end{array} \tag{S63}$$

where $T(\boldsymbol{n}, \boldsymbol{t})$ is the refraction coefficient, $M = 3$, $n_{M+1} = n_0$.

The constrained nonlinear optimization problem is solved numerically by calling the MATLAB function ”`fmincon`” with given random initial conditions satisfying the constraints, where the sequential quadratic programming (SQP) algorithm is implemented.

14. RESISTOR FUNCTIONS IN SMART WAVEFORM MORPHING AND INFORMATION

In the main text, the transfer functions can be modulated into various forms, such as sinusoidal functions and smooth step functions for smart waveform morphing and information coding. The sinusoidal function of the resistor in Fig. 6b of the main text is

$$R_1(t) = 5.3 + 0.1 \cos \frac{2\pi t}{T} \tag{S64}$$

where $T = 0.2$ s. The smooth step function of the resistor in Fig. 6e of the main text is

$$R_1(t) = \begin{cases} 5.2 & 0 \leq t \leq \frac{T-\Delta T}{2} \\ 0.2 \times \frac{t-mT/2+\Delta T/2}{\Delta T} + 5.2 & \frac{mT-\Delta T}{2} \leq t \leq \frac{mT+\Delta T}{2} \\ 5.4 & \frac{mT+\Delta T}{2} \leq t \leq mT - \frac{\Delta T}{2} \\ -0.2 \times \frac{t-mT+\Delta T/2}{\Delta T} + 5.4 & mT - \frac{\Delta T}{2} \leq t \leq mT + \frac{\Delta T}{2} \\ 5.2 & mT + \frac{\Delta T}{2} \leq t \leq \frac{3mT}{2} - \frac{\Delta T}{2} \\ 0.2 \times \frac{t-3mT/2+\Delta T/2}{\Delta T} + 5.2 & \frac{3mT-\Delta T}{2} \leq t \leq \frac{3mT+\Delta T}{2} \end{cases}, \quad m = 1, 2, 3..., \tag{S65}$$

where $T = 0.2$ s and $\Delta T = 0.02$ s. The smooth step function of the resistor in Fig. 7b of the main text is

$$R_1(t) = \begin{cases} 5.2 & 0 \leq t \leq \frac{2T-\Delta T}{2} \\ 0.2 \times \frac{t-T+\Delta T/2}{\Delta T} + 5.2 & \frac{T-\Delta T}{2} \leq t \leq \frac{2T+\Delta T}{2} \\ 5.4 & \frac{2T+\Delta T}{2} \leq t \leq \frac{3T-\Delta T}{2} \\ -0.08 \times \frac{t-3T+\Delta T/2}{\Delta T} + 5.4 & \frac{3T-\Delta T}{2} \leq t \leq 2T + \frac{\Delta T}{2} \\ 5.32 & 2T + \frac{\Delta T}{2} \leq t \leq \frac{5T}{2} - \frac{\Delta T}{2} \\ -0.12 \times \frac{t-5T/2+\Delta T/2}{\Delta T} + 5.32 & \frac{5T-\Delta T}{2} \leq t \leq \frac{5T+\Delta T}{2} \\ 5.2 & \frac{5T-\Delta T}{2} \leq t \leq 3T \end{cases}, \tag{S66}$$

where $T = 0.2$ s and $\Delta T = 0.02$ s. The values 5.2 kΩ, 5.3 kΩ, and 5.4 kΩ were chosen based on a balance between functional performance and system stability:

- **5.2 kΩ** marks the point at which the effective bending stiffness begins to become negative, which leads to significant amplitude gain and thus is useful for distinguishing the ”dash” signal.
- **5.4 kΩ** is the highest resistance we can apply before the system becomes unstable due to excessive feedback-induced amplification in the circuit.
- **5.3 kΩ** serves as a middle setting that produces a clearly distinguishable amplitude between the 5.2 and 5.4 kΩ cases, and is assigned to the ”dot” signal in Morse coding.

Additional information

Supplementary information The online version contains supplementary material available at https://doi.org/10.1038/s41467-025-64530-8.

Correspondence and requests for materials should be addressed to Andrea Alú or Guoliang Huang.

Peer review information *Nature Communications* thanks Junsuk Rho and the other, anonymous, reviewer(s) for their contribution to the peer review of this work. A peer review file is available.